PAN ARCHIVES OF ACOUSTICS
Vol. **40**, No. 3, pp. 359–381 (2015)

DOI: 10.1515/aoa-2015-0039

Active Transient Sound Radiation Control from a Smart Piezocomposite Hollow Cylinder

Seyyed M. HASHEMINEJAD, Vahid RABBANI

Acoustics Research Laboratory, Center of Excellence in Experimental Solid Mechanics and Dynamics
School of Mechanical Engineering, Iran University of Science and Technology
Narmak, Tehran 16846-13114 Iran; e-mail: hashemi@iust.ac.ir

(*received August 4, 2014; accepted June 25, 2015*)

The linear 3D piezoelasticity theory along with active damping control (ADC) strategy are applied for non-stationary vibroacoustic response suppression of a doubly fluid-loaded functionally graded piezolaminated (FGPM) composite hollow cylinder of infinite length under general time-varying excitations. The control gain parameters are identified and tuned using Genetic Algorithm (GA) with a multi-objective performance index that constrains the key elasto-acoustic system parameters and control voltage. The uncontrolled and controlled time response histories due to a pair of equal and opposite impulsive external point loads are calculated by means of Durbin's numerical inverse Laplace transform algorithm. Numerical simulations demonstrate the superior (good) performance of the GA-optimized distributed active damping control system in effective attenuation of sound pressure transients radiated into the internal (external) acoustic space for two basic control configurations. Also, some interesting features of the transient fluid-structure interaction control problem are illustrated via proper 2D time domain images and animations of the 3D sound field. Limiting cases are considered and accuracy of the formulation is established with the aid of a commercial finite element package as well as comparisons with the current literature.

Keywords: active structural acoustic control (ASAC) thick cylindrical shells, exact elasto-acoustic analysis, time-domain solution, intelligent system, sound field attenuation.

1. Introduction

Prediction of time-dependent acoustic behaviour of fluid-coupled structures have been the subject of current research as the most external excitations or acoustic pressure signals in many technological and engineering applications are of transient nature (Hasheminejad *et al.*, 2011; 2012; Hasheminejad, Mousavi-akbarzadeh, 2013). In particular, the non-stationary fluid-structure interaction of submerged cylindrical shell structures experiencing weak shock loads or wideband mechanical excitations is a challenging multi-physics problem of fundamental value that has been widely investigated over the past several decades (Hasheminejad, Mousavi-akbarzadeh, 2013; Leblond, Sigrist, 2010; Iakovlev *et al.*, 2012; 2013). Suppression of sound radiation from these structures based on the traditional passive control methods (Hasheminejad *et al.*, 2008; Hasheminejad, Kazemirad, 2008) is generally inadequate due to the degradation of the damping characteristics of such treatments under temperature and frequency deviations in addition to the cost of adding considerable weight or volume to the vibrating structure. Recent advances in the field of smart material technology in conjunction with the significant improvements in the computational ability of microcomputers have provided efficient means to reduce vibration and acoustic emission of distributed parameter structural systems (Crawley, de Luis, 1987; Hasheminejad, Alaei-Varnosfaderani, 2012; 2013; Hasheminejad, Keshavarzpour, 2013). In particular, the coupled electromechanical properties of piezoelectric materials integrated into the conventional structures allow them to convert electrical energy to mechanical energy and *vice versa*, making these materials appropriate for use as piezoelectric sensor and actuator layers in a broad range of practical applications in active vibration and noise control (Chopra, 2002; Alkhatib, Golnaraghi, 2003; Gabbert, Tzou, 2001). In what follows, an exhaustive review is avoided and we shall briefly review the most relevant key contributions re-

garding active vibration and sound radiation control of submerged cylindrical shell structures.

Numerous authors have recently employed various control methods to improve dynamic characteristics of fluid-coupled cylindrical structures as the basic element in many engineering and industrial applications (e.g. submarine hulls, aircraft fuselage, rockets, torpedoes, machine casings, pressure vessels, ducts, etc. (Hasheminejad, Alaei-Varnosfaderani, 2012; 2013; Hasheminejad, Keshavarzpour, 2013; Su *et al.*, 2010; Sarangi, Ray, 2011; Kumar, Ray, 2013; Ray, Reddy, 2013; Hasheminejad, Rajabi, 2008). For example, Clark and Fuller (1994) carried out narrow-band acoustic control experiments to show that piezoceramic (PZT) actuators and surface-mounted polyvinylidene fluoride (PVDF) structural sensors along with the filtered-X LMS (Least Mean Square) algorithm can be used for active structural acoustic control of a long and thin aluminum cylinder. Wang and Vaicaitis (1998) considered active control of noise transmission into double wall composite cylindrical shells under random pressure and point loadings by using pairs of spatially discrete piezoelectric actuators. They observed that direct velocity feedback control could provide major reduction of vibration and noise levels. Maillard and Fuller (1999) presented analytical and experimental results where Discrete Structural Acoustic Sensing (DSAS) technique was developed for broadband active control of the sound radiation from a submerged cylinder by using arrays of surface mounted point sensors (accelerometers) and piezoelectric actuators implemented through a multi-channel Filtered x-LMS control algorithm. Song *et al.* (2000) considered experimental design of controllers to reduce radiated noise from a very stiff thick-walled shell by actively controlling the shell's outer surface motion by means of an array of surface-mounted curved active composite panels in MIMO configuration. Ruzzene and Baz (2000) used a finite element model to control sound radiation and power flow of fluid-loaded shells using multiple stiffening rings with hybrid active/passive treatments. Laplante *et al.* (2002) used finite element modelling along with experiments to demonstrate vibrational and acoustic performance of submerged cylindrical shells with patches of Active Constrained Layer Damping (ACLD) treatments over a broad frequency band. An underwater hydrophone was used to generate the sensor output voltage and proportional derivative feedback control was applied to the ACLD patches. Thorp *et al.* (2005) adopted a finite element model to study and control the vibration and sound radiation of fluid-loaded cylindrical shells with periodically placed shunted piezoelectric rings. Zhang *et al.* (2006) employed the Mindlin theory, the governing equations of linear piezoelectricity, the fluid dynamic equations for an ideal and incompressible fluid, along with the GHM (Golla-Hughes-McTavish) viscoelastic materials model for finite element modelling of a moderately thick fluid-filled cylindrical shell with ACLD. Pan *et al.* (2008) employed T-sectioned circumferential stiffeners driven by pairs of PZT stack actuators to study the use of piezoelectric moment to control the low frequency radiated pressure from a cylindrical submarine hull under an axial excitation. Hasheminejad and Rajabi (2008) used the spatial state-space approach in conjunction with the Resonance Scattering Theory (RST) to formulate a three-dimensional exact solution for sound wave scattering and active cancellation from an arbitrarily thick piezoelectric-coupled orthotropic hollow cylinder submerged in and filled with compressible acoustic fluids. Caresta (2011) proposed the use of inertial actuators, arranged in circumferential arrays, to reduce sound radiation form a ring-stiffened submarine hull structure in bending vibrations caused by harmonic radial excitations from the propeller. Xiang *et al.* (2011) employed the so-named extended homogeneous capacity precision integration method to present a semi-analytic solution for the previously derived electric-fluid-structure coupled governing equations of a liquid-filled circular cylindrical shell treated with piezoelectric active constrained layer damping layers, and subject to ground harmonic motion. Jin *et al.* (2011) presented a numerical and experimental study on active structural acoustic control (ASAC) of sound radiation from a vibrating elastic cylindrical shell by a local control strategy using optimal point forces as control inputs and minimization of the mean-square velocity of finite discrete locations. Kwak *et al.* (2012) employed the Rayleigh-Ritz method based on the Donnell-Mushtari shell theory and positive position feedback control to investigate the active vibration and sound radiation control of a submerged baffled cylindrical shell by using piezoelectric sensors and actuators. Cao *et al.* (2012) employed a pair of surface-mounted in-phase-driven piezoelectric stack force actuators for active vibration and low-frequency sound radiation control of a fluid-loaded stiffened cylindrical hull of finite length with rigid end-caps under axial mechanical excitations. Just recently, Kwak and Yang (2013) both theoretically and experimentally investigated active vibration and sound radiation control of a ring-stiffened baffled circular cylindrical shell subjected to harmonic disturbance by means of piezoelectric sensor and actuator pairs. Cao *et al.* (2013) subsequently investigated active (proportional derivative negative feedback) control of sound radiation from laminated cylindrical shells integrated with a segmented piezoelectric actuator layer in the wavenumber domain, based on the first-order shear deformation theory. Kim *et al.* (2013) used finite element and experimental modeling to investigate active vibration and structure-borne noise suppression of an underwater cylindrical shell structure based on

an optimal (LQG) control algorithm in conjunction with Macro Fiber Composites (MFCs) as actuators and sensors. Shen *et al.* (2013) utilized a finite element method in conjunction with certain active control strategies (e.g. the inverted displacement-, velocity- and acceleration-feedback control) to suppress the internal/external acoustic pressure fields in hybrid periodic cylindrical shell systems. Hasheminejad and Alaei-Varnosfaderani (2013) used the linear 3D piezoelasticity theory and the method of stationary phase to investigate harmonic far-field acoustic radiation suppression from a doubly-fluid-loaded infinitely-long arbitrary-thick functionally graded piezocomposite hollow cylinder.

The above review clearly shows that, while there are a wealth of research efforts that take advantage of the piezoelectric sensor/actuator materials to control sound radiation from thin or moderately thick cylindrical shell structures based on various thin/thick shell theories, there seem to be no rigorous studies on *full active* three-dimensional transient vibroacoustic response control of a submerged smart piezocomposite cylindrical shell with arbitrary wall thickness. Accordingly, in this work, we shall extend the basic steady-state elasto-acoustic formulation presented in (Hasheminejad, Alaei-Varnosfaderani, 2013) to the time domain, and employ the active damping control (ADC) methodology with multi-objective GA-based tuning in two distinct control configurations, to fill this important gap in the literature. Such analysis is not limited by the various assumptions made in classical and refined shell theories, and is capable of offering consistent solutions as well as revealing the physical characteristics of the problem (Ding, Chen, 2001). The proposed model is of both academic and industrial interest because of its intrinsic significance as a canonical problem in structural acoustics. The presented time domain methodology can provide deep physical insight into the space-time sound radiation properties of such smart structures, particularly those for which experimental data is not available yet. It can assist in constructing the groundwork for future research, including a range of visualization techniques and computer codes for transient fluid-structure interaction control of mechanically excited cylindrical components, with potential applications in chemical industries, nuclear power plants, marine structures, underwater gas pipelines, and submarine/offshore installations (Lester, Lefebvre, 1993; Clark, Fuller, 1994; Niezrecki, Cudney, 2001). The presented accurate set of solutions can also accompany the general research on the submerged hollow cylindrical piezoelectric elements used for generation and detection of acoustic power in a wide range of practical applications in underwater acoustics and industrial macro-sonics (Vovk, Oliynik, 1996; Balabaev, Ivina 1999; Babaev, Babaev, 2005; Babaev *et al.*, 2010; Wilson, 1988). Lastly, the extensive space-time near-field data can serve as a benchmark for verification of strictly numerical or asymptotic approaches.

2. Formulation

Let us consider a hollow infinite laminated piezocomposite cylinder in two distinct configurations as displayed in Fig. 1. In the first configuration (config. 1), it is composed of a functionally graded orthotropic material (FGOM) inner layer of total thickness $H_{\rm o} = a_{q_{\rm o}} - a_0$, perfectly bonded to an outer radially polarized functionally graded piezoelectric material (FGPM) outer actuator layer of total thickness $H_{\rm a} = a_{q_{\rm o}+q_{\rm a}} - a_{q_{\rm o}}$. In the second configuration (config. 2), it is composed of a functionally graded orthotropic material (FGOM) core layer of total thickness $H_{\rm o} = a_{q_{\rm s}} + q_{\rm o} - a_{q_{\rm s}}$, perfectly joined to inner/outer radially polarized functionally graded piezoelectric material (FGPM) sensor/actuator layers of total thickness $H_{\rm s} = a_{q_{\rm s}} - a_0$ and $H_{\rm a} = a_{q_{\rm s}+q_{\rm o}+q_{\rm a}} - a_{q_{\rm s}+q_{\rm o}}$. The infinite cylinders are supposed to be submerged in and filled with ideal compressible fluids of density $\rho_{\rm ex}$ and $\rho_{\rm in}$, respectively. They are also acted upon by radial time-dependent distributed loads at their external and/or internal surfaces ($F_{\rm ex}$, $F_{\rm in}$), with the corresponding subtending angle and load span denoted by ($\alpha_{\rm ex}$, $d_{\rm ex}$) and ($\alpha_{\rm in}$, $d_{\rm in}$) respectively (see Fig. 1). Before outlining the control strategy, we shall address the structural acoustic model in the next three subsections.

2.1. Structural model

The generalized constitutive equations relating the stress components (Σ_{ij}, σ_{ij}) to the relevant strain components (Γ_{ij}, γ_{ij}) in the functionally graded orthotropic and piezoelectric layers are respectively written as (Ding, Chen, 2001)

$$\begin{aligned} \boldsymbol{\sigma} &= \mathbf{c}\boldsymbol{\gamma}, \\ \boldsymbol{\Sigma} &= \mathbf{C}\boldsymbol{\Gamma} - \mathbf{e}\mathbf{E}, \end{aligned} \tag{1}$$

where

$$\boldsymbol{\sigma} = [\sigma_{\theta\theta} \;\; \sigma_{zz} \;\; \sigma_{rr} \;\; \sigma_{rz} \;\; \sigma_{r\theta} \;\; \sigma_{\theta z}]^{\rm T},$$

$$\boldsymbol{\Sigma} = [\Sigma_{\theta\theta} \;\; \Sigma_{zz} \;\; \Sigma_{rr} \;\; \Sigma_{rz} \;\; \Sigma_{r\theta} \;\; \Sigma_{\theta z}]^{\rm T},$$

$$\mathbf{E} = [\partial\phi/r\partial\theta \;\; \partial\phi/\partial z \;\; \partial\phi/\partial r]^{\rm T}$$

is the electric intensity vector, in which $\phi(r,\theta,z,t)$ is the electric potential, and the radially-dependent elastic and piezoelectric constant matrices ($\mathbf{c}$, $\mathbf{C}$, $\mathbf{e}$) are given in Appendix A. Also, the strain component vectors for the orthotropic and piezoelectric layers,

$$\boldsymbol{\gamma} = [\gamma_{\theta\theta} \;\; \gamma_{zz} \;\; \gamma_{rr} \;\; \gamma_{rz} \;\; \gamma_{r\theta} \;\; \gamma_{\theta z}]^{\rm T}$$

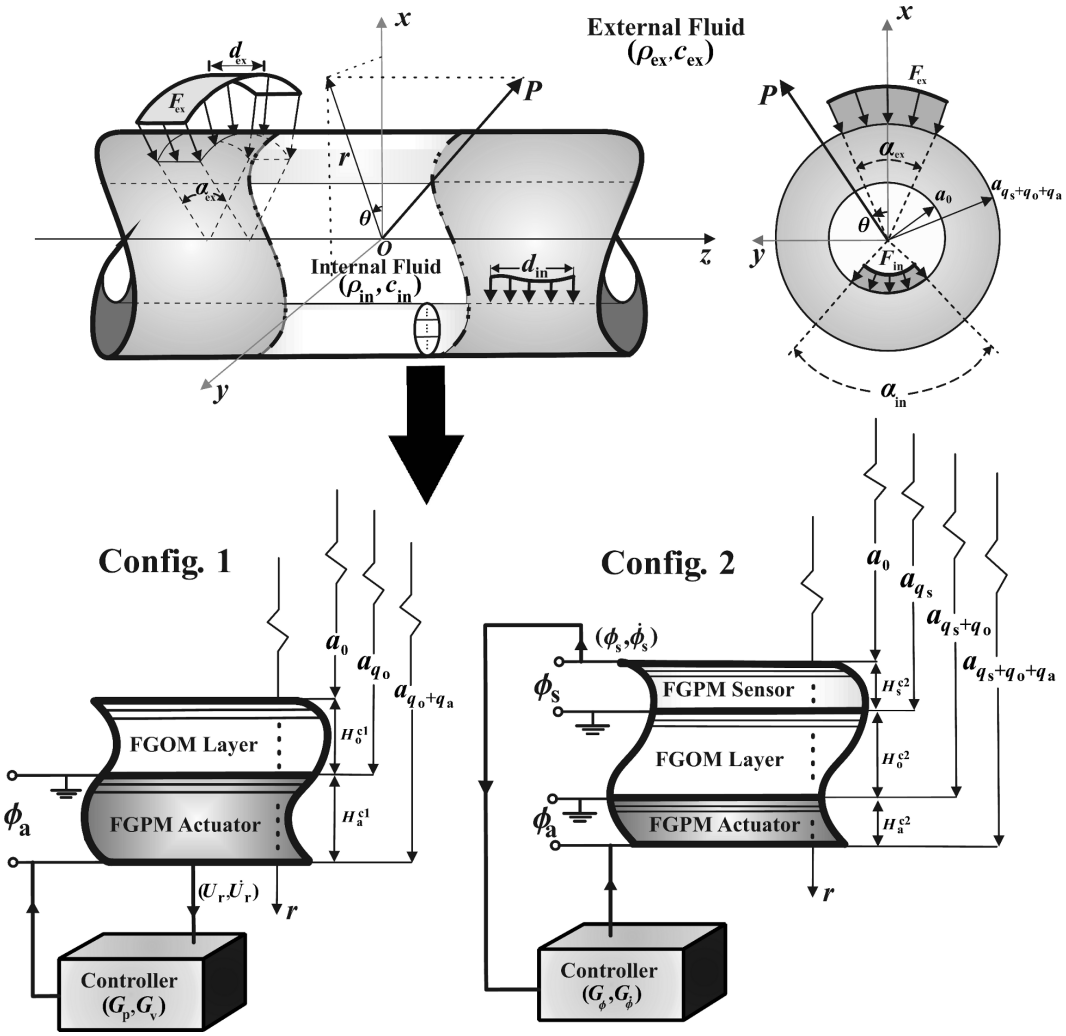

Fig. 1. Problem configuration.

and

$$\boldsymbol{\Gamma} = [\Gamma_{\theta\theta} \;\; \Gamma_{zz} \;\; \Gamma_{rr} \;\; \Gamma_{rz} \;\; \gamma_{r\theta} \;\; \Gamma_{\theta z}]^{\mathrm{T}}$$

are respectively related to the associated material displacement vectors through the classic relation

$$\boldsymbol{\gamma} = \mathbf{K}\mathbf{u}, \qquad \boldsymbol{\Gamma} = \mathbf{K}\mathbf{U}, \tag{2}$$

where $\mathbf{u} = [u_r \;\; u_\theta \;\; u_z]^{\mathrm{T}}$ and $\mathbf{U} = [U_r \;\; U_\theta \;\; U_z]^{\mathrm{T}}$ and the matrix operator $\mathbf{K}$ is given in Appendix A. Moreover, by applying Laplace transform with respect to the time variable in the general form $\overline{\Lambda}(r,\theta,z,s) = \int_0^\infty \Lambda(r,\theta,z,t)e^{-st}\,\mathrm{d}t$ with s being the transform parameter (assuming zero initial conditions), the transformed governing equations of motion for the orthotropic and piezoelectric layers, in the absence of body forces, are respectively written as (Ding, Chen, 2001)

$$\begin{aligned} \mathbf{p}\overline{\boldsymbol{\sigma}} &= \rho_{\mathrm{o}} s^2 \overline{\mathbf{u}}, \\ \mathbf{P}\begin{bmatrix} \overline{\boldsymbol{\Sigma}} \\ \overline{\mathbf{D}} \end{bmatrix} &= \rho_{\mathrm{p}} s^2 \begin{bmatrix} \overline{\mathbf{U}} \\ \overline{Q}_f/\rho_{\mathrm{p}} s^2 \end{bmatrix}, \end{aligned} \tag{3}$$

where $\overline{\mathbf{D}} = \begin{bmatrix} \overline{D}_r & \overline{D}_\theta & \overline{D}_z \end{bmatrix}^{\mathrm{T}}$ and $(\rho_{\mathrm{o}}, \rho_{\mathrm{p}})$ denote the densities of the orthotropic and piezoelectric materials respectively, $\overline{Q}_f$ is the free charge density, the matrix operators $(\mathbf{p}, \mathbf{P})$ are given in Appendix A, and the Laplace transformed electric displacement vector components are given as (Yu *et al.*, 2009)

$$\overline{\mathbf{D}} = \mathbf{e}^{\mathrm{T}}\overline{\boldsymbol{\Gamma}} + \boldsymbol{\varepsilon}\overline{\mathbf{E}}, \tag{4}$$

where the dielectric constant matrix $\boldsymbol{\varepsilon}$ is given in Appendix A.

Subsequent application of the spatial Fourier transform with respect to the axial coordinate, $\widetilde{\overline{\Lambda}}(r,\theta,\xi,s) = \int_{-\infty}^{\infty} \overline{\Lambda}(r,\theta,z,s)e^{-\mathrm{i}\xi z}\,\mathrm{d}z$, where ξ is the Fourier transform parameter (Hilderbrand, 1992), transforms the governing Eqs. (1) through (4) into the Fourier domain. The full 3D analysis of the hollow piezocomposite cylinder is a challenging task. As the cylinder geometry is constant along its axis, one can express the three-dimensional solution as a discrete summation of simpler two-dimensional solutions

with different spatial wave numbers (Hasheminejad, Mousavi-akbarzadeh, 2013). In particular, the inverse Fourier transform integral can be expediently handled by supposition of a series of equally spaced virtual loads of inter-distance, L, along cylinder axis. Therefore, the (Laplace) transformed spatial state vectors associated with the orthotropic and piezoelectric layers, $\mathbf{v} = [\overline{u}_r \;\; \overline{u}_\theta \;\; \overline{u}_z \;\; \overline{\sigma}_{rr} \;\; \overline{\sigma}_{r\theta} \;\; \overline{\sigma}_{rz}]^{\mathrm{T}}$, $\mathbf{V} = [\overline{U}_r \;\; \overline{U}_\theta \;\; \overline{U}_z \;\; \overline{\Sigma}_{rr} \;\; \overline{\Sigma}_{r\theta} \;\; \overline{\Sigma}_{rz} \;\; \overline{D}_r \;\; \overline{\phi}]^{\mathrm{T}}$, may advantageously be expanded in terms of the pertinent modal coefficients in the form (Hasheminejad, Mousavi-akbarzadeh, 2013):

$$\mathbf{v} = \sum_{n=-\infty}^{\infty}\sum_{m=-\infty}^{\infty} \begin{Bmatrix} \overline{u}_r^{nm}(r,s)\cos(n\theta) \\ \overline{u}_\theta^{nm}(r,s)\sin(n\theta) \\ \overline{u}_z^{nm}(r,s)\cos(n\theta) \\ \overline{\sigma}_{rr}^{nm}(r,s)\cos(n\theta) \\ \overline{\sigma}_{r\theta}^{nm}(r,s)\sin(n\theta) \\ \overline{\sigma}_{rz}^{nm}(r,s)\cos(n\theta) \end{Bmatrix} e^{\mathrm{i}\xi_m z},$$

$$\mathbf{V} = \sum_{n=-\infty}^{\infty}\sum_{m=-\infty}^{\infty} \begin{Bmatrix} \overline{U}_r^{nm}(r,s)\cos(n\theta) \\ \overline{U}_\theta^{nm}(r,s)\sin(n\theta) \\ \overline{U}_z^{nm}(r,s)\cos(n\theta) \\ \overline{\Sigma}_{rr}^{nm}(r,s)\cos(n\theta) \\ \overline{\Sigma}_{r\theta}^{nm}(r,s)\sin(n\theta) \\ \overline{\Sigma}_{rz}^{nm}(r,s)\cos(n\theta) \\ \overline{D}_r^{nm}(r,s)\cos(n\theta) \\ \overline{\phi}_{nm}(r,s)\cos(n\theta) \end{Bmatrix} e^{\mathrm{i}\xi_m z}, \tag{5}$$

where $\mathrm{i} = \sqrt{-1}$ and $\xi_m = 2m\pi/L$. Now, by direct substitution of the constitutive relations (1), (2), (4) and expansion (5) into the transformed equations of motion (3), and utilizing the classical orthogonality of trigonometric functions, the spatial (modal) state equations for the FGOM and FGPM layers are respectively obtained as

$$\begin{aligned} \frac{\mathrm{d}\mathbf{v}_{nm}}{\mathrm{d}r} &= \mathbf{g}_{nm}\mathbf{v}_{nm}, \\ \frac{\mathrm{d}\mathbf{V}_{nm}}{\mathrm{d}r} &= \mathbf{G}_{nm}\mathbf{V}_{nm}, \end{aligned} \tag{6}$$

where

$$n,\ m = -\infty, \ldots, 0 \ldots, \infty,$$

$$\mathbf{v}_{nm} = [\overline{u}_r^{nm} \;\; \overline{u}_\theta^{nm} \;\; \overline{u}_z^{nm} \;\; \overline{\sigma}_{rr}^{nm} \;\; \overline{\sigma}_{r\theta}^{nm} \;\; \overline{\sigma}_{rz}^{nm}]^{\mathrm{T}}$$

and

$$\mathbf{V}_{nm} = \left[\overline{U}_r^{nm} \;\; \overline{U}_\theta^{nm} \;\; \overline{U}_z^{nm} \;\; \overline{\Sigma}_{rr}^{nm} \;\; \overline{\Sigma}_{r\theta}^{nm} \;\; \overline{\Sigma}_{rz}^{nm} \;\; \overline{D}_r^{nm} \;\; \overline{\phi}_{nm}\right]^{\mathrm{T}}$$

are the modal state vectors, and $\mathbf{g}_{nm}(r,s)$ and $\mathbf{G}_{nm}(r,s)$ are 6×6 and 8×8 modal coefficient matrices whose elements are given in Appendix B, respectively.

The elements of $\mathbf{g}_{nm}$ and $\mathbf{G}_{nm}$ are position dependent. Hence, direct solution of state Eqs. (6) is very difficult. Adopting an approximate laminate model (Ding, Chen, 2001), we assume that the FGOM layer in the first and second configurations (see Fig. 1) are composed of q_{o} perfectly bonded sub-layers of equal thickness, $\widehat{H}_{\mathrm{o}}^{\mathrm{c}1} = (a_{q_{\mathrm{o}}} - a_0)/q_{\mathrm{o}}$, and $\widehat{H}_{\mathrm{o}}^{\mathrm{c}2} = (a_{q_{\mathrm{s}}+q_{\mathrm{o}}} - a_{q_{\mathrm{s}}})/q_{\mathrm{o}}$, respectively. Similarly, the FGPM actuator and sensor layers may be respectively assumed to be composed of q_{a} and q_{s} perfectly bonded sub-layers of equal thicknesses, $\widehat{H}_{\mathrm{a}}^{\mathrm{c}2} = (a_{q_{\mathrm{s}}+q_{\mathrm{o}}+q_{\mathrm{a}}} - a_{q_{\mathrm{s}}+q_{\mathrm{o}}})/q_{\mathrm{a}}$ and $\widehat{H}_{\mathrm{s}}^{\mathrm{c}2} = (a_{q_{\mathrm{s}}} - a_0)/q_{\mathrm{s}}$ in the second configuration, and q_{a} perfectly bonded actuator sub-layers of equal thickness $\widehat{H}_{\mathrm{a}}^{\mathrm{c}1} = (a_{q_{\mathrm{o}}+q_{\mathrm{a}}} - a_{q_{\mathrm{o}}})/q_{\mathrm{a}}$ in the first configuration (see Fig. 1). As the thickness of each sub-layer is assumed to be very small, the coefficient matrices $\mathbf{g}_{nm}$ and $\mathbf{G}_{nm}$ can favorably be assumed constant within each sub-layer, where one should use its value at the middle radius of the k-th sub-layer (i.e. at $\overline{r}_k = (r_k + r_{k-1})/2$). Thus, within the k-th orthotropic sub-layer, solution to the modal state Eq. $(6)_1$ can be written as

$$\begin{aligned} \mathbf{v}_{nm}(r,s) \;=\; & \exp\left[(r - r_{k-1})\mathbf{g}_{nm}(\overline{r}_k, s)\right]\mathbf{v}_{nm}(r_{k-1}, s), \\ & k = 1, 2, \ldots, q_{\mathrm{o}}, \end{aligned} \tag{7}$$

where

$$r_{k-1} = [a_0 + (k-1)\widehat{H}_{\mathrm{o}}^{\mathrm{c}1}] \le r \le r_k = (a_0 + k\widehat{H}_{\mathrm{o}}^{\mathrm{c}1})$$

for the first configuration, and

$$r_{k-1} = [a_{q_{\mathrm{s}}} + (k-1)\widehat{H}_{\mathrm{o}}^{\mathrm{c}2}] \le r \le r_k = (a_{q_{\mathrm{s}}} + k\widehat{H}_{\mathrm{o}}^{\mathrm{c}2})$$

for the second configuration. Similarly, within the k-th piezoelectric sub-layer, solution to the modal state Eq. $(6)_2$ can be written as

$$\mathbf{V}_{nm}(r,s) = \exp[(r - r_{k-1})\mathbf{G}_{nm}(\overline{r}_k, s)]\mathbf{V}_{nm}(r_{k-1}, s), \tag{8}$$

where $r_{k-1} = [a_0 + (k-1)\widehat{H}_{\mathrm{s}}^{\mathrm{c}2}] \le r \le r_k = (a_0 + k\widehat{H}_{\mathrm{s}}^{\mathrm{c}2})$ for the inner sensor layer in the second configuration ($k = 1, 2, \ldots, q_{\mathrm{s}}$), and $r_{k-1} = [a_{q_{\mathrm{o}}+q_{\mathrm{a}}} + (k-1)\widehat{H}_{\mathrm{a}}^{\mathrm{c}1}] \le r \le r_k = (a_{q_{\mathrm{o}}+q_{\mathrm{a}}} + k\widehat{H}_{\mathrm{a}}^{\mathrm{c}1})$, and $r_{k-1} = [a_{q_{\mathrm{s}}+q_{\mathrm{o}}} + (k-1)\widehat{H}_{\mathrm{a}}^{\mathrm{c}2}] \le r \le r_k = (a_{q_{\mathrm{s}}+q_{\mathrm{o}}} + k\widehat{H}_{\mathrm{a}}^{\mathrm{c}2})$ for the actuator layers in the first and second configurations ($k = 1, 2, \ldots, q_{\mathrm{a}}$), respectively. Subsequent evaluations of state solutions (7) and (8) at the outer surfaces of the k-th sub-layer, lead to the following useful recurrence relations for the FGOM and FGPM (sensor and actuator) layers in the first and second configurations, respectively:

$$\begin{aligned} \mathbf{v}_{nm}(r_k, s) &= \exp\left[\widehat{H}_{\mathrm{o}}^{\mathrm{c}1}\mathbf{g}_{nm}(\overline{r}_k, s)\right]\mathbf{v}_{nm}(r_{k-1}, s), \\ \mathbf{V}_{nm}^{\mathrm{a}}(r_k, s) &= \exp\left[\widehat{H}_{\mathrm{a}}^{\mathrm{c}1}\mathbf{G}_{nm}^{\mathrm{a}}(\overline{r}_k, s)\right]\mathbf{V}_{nm}^{\mathrm{a}}(r_{k-1}, s), \quad \text{(config. 1)}, \end{aligned} \tag{9}_1$$

and

$$\begin{aligned}
\mathbf{v}_{nm}(r_k,s) &= \exp\left[\widehat{H}_{\rm o}^{\rm c2}\mathbf{g}_{nm}(\overline{r}_k,s)\right]\mathbf{v}_{nm}(r_{k-1},s),\\
\mathbf{V}_{nm}^{\rm s}(r_k,s) &= \exp\left[\widehat{H}_{\rm s}^{\rm c2}\mathbf{G}_{nm}^{\rm s}(\overline{r}_k,s)\right]\mathbf{V}_{nm}^{\rm s}(r_{k-1},s),\\
\mathbf{V}_{nm}^{\rm a}(r_k,s) &= \exp\left[\widehat{H}_{\rm a}^{\rm c2}\mathbf{G}_{nm}^{\rm a}(\overline{r}_k,s)\right]\mathbf{V}_{nm}^{\rm a}(r_{k-1},s),\\
&\qquad\qquad\text{(config. 2).}
\end{aligned} \tag{9}_2$$

Also, by invoking the continuity conditions between all interface layers within the FGOM medium, the state variables at the outer radii of the FGOM layers for the first and second configuration (i.e., at $r=a_{q_{\rm o}}$ and $r=a_{q_{\rm s}+q_{\rm o}}$) are conveniently related to those at the inner radii (i.e., at $r=a_0$ and $r=a_{q_{\rm s}}$), via 6×6 global modal transfer matrices by the following relations

$$\begin{aligned}
\mathbf{v}_{nm}(a_{q_{\rm o}},s) &= \mathbf{t}_{nm}^{\rm c1}(s)\mathbf{v}(a_0,s), \quad \text{(config. 1)},\\
\mathbf{v}_{nm}(a_{q_{\rm s}+q_{\rm o}},s) &= \mathbf{t}_{nm}^{\rm c2}(s)\mathbf{v}(a_{q_{\rm s}},s), \quad \text{(config. 2)},
\end{aligned} \tag{10}$$

where $\mathbf{t}_{nm}^{ci}=\prod\limits_{k=1}^{q_{\rm o}}\exp\left[\widehat{H}_{\rm o}^{ci}\mathbf{g}_{nm}(\overline{r}_k,s)\right]$ $(i=1,\,2)$. Similarly, by invoking the continuity conditions between all interface layers, the state variables at the outer radii of the FGPM actuator layers for the first and second configurations (i.e. at $r=a_{q_{\rm o}+q_{\rm a}}$ and $r=a_{q_{\rm s}+q_{\rm o}+q_{\rm a}}$) are beneficially related to those at the inner radii (i.e. at $r=a_{q_{\rm o}}$ and $r=a_{q_{\rm s}+q_{\rm o}}$), via 8×8 global modal transfer matrices by

$$\begin{aligned}
\mathbf{V}_{nm}^{\rm a}(a_{q_{\rm o}+q_{\rm a}},s) &= \mathbf{T}_{nm}^{\rm ac1}(s)\mathbf{V}_{nm}^{\rm a}(a_{q_{\rm o}},s) \quad \text{(config. 1)},\\
\mathbf{V}_{nm}^{\rm a}(a_{q_{\rm s}+q_{\rm o}+q_{\rm a}},s) &= \mathbf{T}_{nm}^{\rm ac2}(s)\mathbf{V}_{nm}^{\rm a}(a_{q_{\rm s}+q_{\rm o}},s) \quad \text{(config. 2)},
\end{aligned} \tag{11}$$

where $\mathbf{T}_{nm}^{{\rm ac}i}=\prod\limits_{k=1}^{q_{\rm a}}\exp\left[\widehat{H}_{\rm a}^{ci}\mathbf{G}_{nm}^{\rm a}(\overline{r}_k,s)\right]$ $(i=1,2)$. Moreover, by invoking the continuity conditions between all sensor sub-layers, the state variables at the outer radii of the FGPM sensor layer in the second configuration (i.e. at $r=a_{q_{\rm s}}$) are usefully related to those at the inner radii (i.e. at $r=a_0$), via 8×8 global modal transfer matrices by

$$\mathbf{V}_{nm}^{\rm s}(a_{q_{\rm s}},s)=\mathbf{T}_{nm}^{\rm sc2}(s)\mathbf{V}_{nm}^{\rm s}(a_0,s), \tag{12}$$

where $\mathbf{T}_{nm}^{\rm sc2}=\prod\limits_{k=1}^{q_{\rm s}}\exp\left[\widehat{H}_{\rm s}^{\rm c2}\mathbf{G}_{nm}^{\rm s}(\overline{r}_k,s)\right]$.

Lastly, adopting the simple rule of mixture to describe the distribution of material properties across the thicknesses of FGOM and FGPM layers (Yu et al., 2009), the relevant elastic constants and mass densities within the k-th layer of inner radius r_{k-1}, and outer radius r_k can be expressed in the form

$$\begin{aligned}
c_{ij}^{(k)} &= c_{ij}(\overline{r}_k) = V_{\rm o}(\overline{r}_k)c_{ij}^{\rm int}+[1-V_{\rm o}(\overline{r}_k)]c_{ij}^{\rm ext}\\
\rho_{\rm o}^{(k)} &= \rho_{\rm o}(\overline{r}_k) = V_{\rm o}(\overline{r}_k)\rho_{\rm o}^{\rm int}+[1-V_{\rm o}(\overline{r}_k)]\rho_{\rm o}^{\rm ext},
\end{aligned} \tag{13}_1$$

and

$$\begin{aligned}
C_{ij}^{(k)} &= C_{ij}(\overline{r}_k) = V_{\rm p}(\overline{r}_k)C_{ij}^{\rm int}+[1-V_{\rm p}(\overline{r}_k)]C_{ij}^{\rm ext},\\
\rho_{\rm p}^{(k)} &= \rho_{\rm p}(\overline{r}_k) = V_{\rm p}(\overline{r}_k)\rho_{\rm p}^{\rm int}+[1-V_{\rm p}(\overline{r}_k)]\rho_{\rm p}^{\rm ext},\\
e_{ij}^{(k)} &= e_{ij}(\overline{r}_k) = V_{\rm p}(\overline{r}_k)e_{ij}^{\rm int}+[1-V_{\rm p}(\overline{r}_k)]e_{ij}^{\rm ext},\\
\varepsilon_{ij}^{(k)} &= \varepsilon_{ij}(\overline{r}_k) = V_{\rm p}(\overline{r}_k)\varepsilon_{ij}^{\rm int}+[1-V_{\rm p}(\overline{r}_k)]\varepsilon_{ij}^{\rm ext},
\end{aligned} \tag{13}_2$$

where the subscript ${\rm p}={\rm s,a}$, (i.e. referring to the sensor or actuator layer), $V_{\rm o}(\overline{r}_k)$ and $V_{\rm p}(\overline{r}_k)=V_{\rm s,a}(\overline{r}_k)$ are the volume fractions of the "internal" material in the k-th mid-sub-layer of the FGOM and FGPM layers, respectively, and $(c_{ij}^{\rm int},\,\rho_{\rm o}^{\rm int})$, $(C_{ij}^{\rm int},\,\rho_{\rm s,a}^{\rm int})$ and $(C_{ij}^{\rm ext},\,\rho_{\rm s,a}^{\rm ext})$, $(c_{ij}^{\rm ext},\,\rho_{\rm o}^{\rm ext})$ are the elastic coefficients and mass densities of internal and external constituting FGOM and FGPM materials, respectively.

2.2. Final global transfer matrix

At this point, by incorporating the perfect bonding conditions at the interface between the FGOM and FGPM actuator layers (i.e. at $r=a_{q_{\rm o}}$) for the first configuration in the state space formulation, the modal state variable vector at inner FGOM layer ($r=a_0$), augmented with the relevant electrical state variables at the inner surface of the actuator layer ($r=a_{q_{\rm o}}$), may advantageously be related to that at the outer radius of the actuator layer ($r=a_{q_{\rm o}+q_{\rm a}}$) via a 8×8 global transfer matrix, $\mathbf{W}_{nm}^{\rm c1}$, in the form

$$\mathbf{V}_{nm}^{\rm a}(a_{q_{\rm o}+q_{\rm a}},s)=\mathbf{W}_{nm}^{\rm c1}(s)\mathbf{X}_{nm}^{\rm c1}(s), \tag{14}$$

in which

$$\mathbf{W}_{nm}^{\rm c1}=[\mathbf{T}_{nm}^{\rm ac1}(:,1{:}6)\mathbf{t}_{nm}^{\rm c1}\quad \mathbf{T}_{nm}^{\rm ac1}(:,7{:}8)]$$

and

$$\mathbf{X}_{nm}^{\rm c1}(s)=\begin{bmatrix}\mathbf{v}_{nm}^{\rm T}(a_0,s)\\ \overline{D}_{r,nm}^{\rm a}(a_{q_{\rm o}},s)\\ \overline{\phi}_{nm}^{\rm a}(a_{q_{\rm o}},s)\end{bmatrix},$$

where it should be noted that $\mathbf{T}_{nm}^{\rm ac1}(:,1{:}6)$ contains only the first six columns of $\mathbf{T}_{nm}^{\rm ac1}$, while $\mathbf{T}_{nm}^{\rm ac1}(:,7{:}8)$ contains only the last two columns of $\mathbf{T}_{nm}^{\rm ac1}$.

Similarly, in the second configuration, the modal state variable vector at the inner surface of FGOM layer ($r=a_{q_{\rm s}}$), augmented with the relevant electrical state variables at the inner surface of the actuator layer ($r=a_{q_{\rm s}+q_{\rm o}}$), may advantageously be related to that at the outer radius of the actuator layer ($r=a_{q_{\rm s}+q_{\rm o}+q_{\rm a}}$) via a 8×8 transfer matrix, $\mathbf{S}_{nm}^{\rm c2}$, in the form

$$\mathbf{V}_{nm}^{\rm a}(a_{q_{\rm s}+q_{\rm o}+q_{\rm a}},s)=\mathbf{S}_{nm}^{\rm c2}(s)\mathbf{X}_{nm}^{\rm c2}(s), \tag{15}$$

in which

$$\mathbf{S}_{nm}^{\rm c2}=\left[\mathbf{T}_{nm}^{\rm ac2}(:,1{:}6)\mathbf{t}_{nm}^{\rm c2}\quad \mathbf{T}_{nm}^{\rm ac2}(:,7{:}8)\right]$$

and

$$\mathbf{X}^{\mathrm{c2}}_{nm}(s) = \begin{bmatrix} \mathbf{v}^{\mathrm{T}}_{nm}(a_{q_\mathrm{s}}, s) \\ \overline{D}^{\mathrm{a}}_{r,nm}(a_{q_\mathrm{s}+q_\mathrm{o}}, s) \\ \overline{\phi}^{\mathrm{a}}_{nm}(a_{q_\mathrm{s}+q_\mathrm{o}}, s) \end{bmatrix}.$$

Moreover, by incorporating the perfect bonding conditions at the interface between the FGOM core and the FGPM sensor layer (i.e. at $r = a_{q_\mathrm{s}}$) in our state space formulation, the modal state variable vector at the inner surface of the sensor layer (i.e. at $r = a_0$), can be related to that at the outer surface of the actuator layer (i.e. at $r = a_{q_\mathrm{s}+q_\mathrm{o}+q_\mathrm{a}}$) via the global transfer matrix, $\mathbf{W}^{\mathrm{c2}}_{nm}(10 \times 10)$, in the form

$$\mathbf{Y}_{nm}(s) = \mathbf{W}^{\mathrm{c2}}_{nm}(s)\mathbf{R}_{nm}(s) \quad (n,\ m = -\infty, \ldots, 0, \ldots, +\infty), \tag{16}$$

where

$$\mathbf{W}^{\mathrm{c2}}_{nm} = \begin{bmatrix} \mathbf{S}^{\mathrm{c2}}_{nm}(:, 1{:}6)\mathbf{T}^{\mathrm{sc2}}_{nm}(1{:}6, :) & \mathbf{S}^{\mathrm{c2}}_{nm}(:, 7{:}8) \\ \mathbf{T}^{\mathrm{sc2}}_{nm}(7{:}8, :) & \mathbf{0} \end{bmatrix},$$

and

$$\mathbf{Y}_{nm} = \begin{bmatrix} \mathbf{V}^{\mathrm{a}}_{nm}(a_{q_\mathrm{s}+q_\mathrm{o}+q_\mathrm{a}}, s) \\ \overline{D}^{\mathrm{s}}_{r,nm}(a_{q_\mathrm{s}}, s) \\ \overline{\phi}^{\mathrm{s}}_{nm}(a_{q_\mathrm{s}}, s) \end{bmatrix},$$

$$\mathbf{R}_{nm} = \begin{bmatrix} \mathbf{V}^{\mathrm{s}}_{nm}(a_0, s) \\ \overline{D}^{\mathrm{a}}_{r,nm}(a_{q_\mathrm{s}+q_\mathrm{o}}, s) \\ \overline{\phi}^{\mathrm{a}}_{nm}(a_{q_\mathrm{s}+q_\mathrm{o}}, s) \end{bmatrix},$$

where it should be noted that $\mathbf{T}^{\mathrm{sc2}}_{nm}(7{:}8, :)$ contains only the last two rows of $\mathbf{T}^{\mathrm{sc2}}_{nm}$.

2.3. Acoustic field equations and mechanical boundary conditions

The basic acoustic field equations governing the sound pressure and radial fluid particle acceleration in the transformed Laplace domain are written as (Pierce, 1991)

$$\nabla^2 \overline{p} = \frac{s^2}{c^2}\overline{p}, \qquad s^2 \overline{v}_r = \frac{1}{\rho}\frac{\partial \overline{p}}{\partial r}, \tag{17}$$

where

$$\nabla^2 = \frac{\partial^2}{\partial r^2} + \frac{1}{r}\frac{\partial}{\partial r} + \frac{1}{r^2}\frac{\partial^2}{\partial \theta^2} + \frac{\partial^2}{\partial z^2}$$

is the Laplacian, ρ is the fluid density, and c is the speed of sound. Also, the acoustic pressure fields in the internal and external ideal compressible fluids (see Fig. 1) may be expanded in the form

$$\overline{p}_{\mathrm{in}}(r, \theta, z, s) = \sum_{m=-\infty}^{\infty}\sum_{n=-\infty}^{\infty} P^{\mathrm{in}}_{nm}(r, s)\cos(n\theta)e^{\mathrm{i}\xi_m z},$$
$$\overline{p}_{\mathrm{ex}}(r, \theta, z, s) = \sum_{m=-\infty}^{\infty}\sum_{n=-\infty}^{\infty} P^{\mathrm{ex}}_{nm}(r, s)\cos(n\theta)e^{\mathrm{i}\xi_m z}, \tag{18}$$

where "in, ex" refer to the quantities in the inner and outer acoustic fluid mediums respectively, and by use first of (17), one has $P^{\mathrm{in}}_{nm}(r, s) = Q^{\mathrm{in}}_{nm} I_n(\tau^{\mathrm{in}}_m r)$ and $P^{\mathrm{ex}}_{nm}(r, s) = Q^{\mathrm{ex}}_{nm} K_n(\tau^{\mathrm{ex}}_m r)$ in which $(\tau^{\mathrm{in,ex}}_m)^2 = (s/c_{\mathrm{in,\,ex}})^2 + \xi^2_m$, $I_n(x)$ and $K_n(x)$ are the modified Bessel functions of the first and second kinds, respectively, $Q^{\mathrm{in}}_{nm} = \rho_{\mathrm{in}} s^2 I_n(\tau^{\mathrm{in}}_m r)/I'_n(\tau^{\mathrm{in}}_m r)$, $Q^{\mathrm{ex}}_{nm} = \rho_{\mathrm{ex}} s^2 K_n(\tau^{\mathrm{ex}}_m r)/K'_n(\tau^{\mathrm{ex}}_m r)$, and "prime" denotes differentiation with respect to the radial coordinate. Similarly, the external radial and transverse loads applied at the inner/outer surfaces of the infinite cylinder (see Fig. 1) may respectively be expanded in the transformed general form

$$\overline{F}_{\mathrm{in}}(\theta, z, s) = \sum_{n=-\infty}^{\infty}\sum_{m=-\infty}^{\infty} F^{nm}_{\mathrm{in}}(s)\cos(n\theta)e^{\mathrm{i}\xi_m z},$$
$$\overline{F}_{\mathrm{ex}}(\theta, z, s) = \sum_{n=-\infty}^{\infty}\sum_{m=-\infty}^{\infty} F^{nm}_{\mathrm{ex}}(s)\cos(n\theta)e^{\mathrm{i}\xi_m z}, \tag{19}$$

where

$$F^{nm}_{\mathrm{in}}(s) = \frac{1}{2\pi L}\int_{-\pi}^{\pi}\int_{0}^{L} \overline{F}_{\mathrm{in}}(\theta, z, s)\cos(n\theta)e^{-\mathrm{i}\xi_m z}\,\mathrm{d}z\,\mathrm{d}\theta,$$

$$F^{nm}_{\mathrm{ex}}(s) = \frac{1}{2\pi L}\int_{-\pi}^{\pi}\int_{0}^{L} \overline{F}_{\mathrm{ex}}(\theta, z, s)\cos(n\theta)e^{-\mathrm{i}\xi_m z}\,\mathrm{d}z\,\mathrm{d}\theta.$$

Now, the pertinent (transformed) mechanical boundary conditions that must be enforced at the inner surface of the FGOM layer and outer surface of the actuator layer in the first configuration are written as:

- vanishing of the tangential stress components at the inner/outer surfaces of the infinite cylinder:

$$\overline{\sigma}^{nm}_{rz}(a_0, s) = \overline{\sigma}^{nm}_{rz}(a_{q_\mathrm{o}+q_\mathrm{a}}, s) = 0,$$
$$\overline{\sigma}^{nm}_{r\theta}(a_0, s) = \overline{\sigma}^{nm}_{r\theta}(a_{q_\mathrm{o}+q_\mathrm{a}}, s) = 0, \tag{20}_1$$

- equilibrium of the normal stress and applied external normal load and fluid pressure at the outer/inner surfaces of the infinite cylinder:

$$\overline{\sigma}^{nm}_{rr}(a_{q_\mathrm{o}+q_\mathrm{a}}, s) = -F^{nm}_{\mathrm{ex}} - P^{\mathrm{ex}}_{nm},$$
$$\overline{\sigma}^{nm}_{rr}(a_0, s) = -F^{nm}_{\mathrm{in}} - P^{\mathrm{in}}_{nm}(a_0, s), \tag{20}_2$$

- continuity of the normal fluid and solid displacements at the inner/outer surfaces of the infinite cylinder:

$$[Q^{\mathrm{in}}_{nm}]^{-1} P^{\mathrm{in}}_{nm}(a_0, s) = \overline{u}^{nm}_r(a_0, s),$$
$$[Q^{\mathrm{ex}}_{nm}]^{-1} P^{\mathrm{ex}}_{nm}(a_{q_\mathrm{o}+q_\mathrm{a}}, s) = \overline{U}^{nm}_r(a_{q_\mathrm{o}+q_\mathrm{a}}, s). \tag{20}_3$$

Similarly, in the second configuration, the appropriate (transformed) mechanical boundary conditions that must be enforced at the inner surface of the sensor layer and outer surface of the actuator layer are given as:

- vanishing of the tangential stress components at the inner/outer surfaces of the infinite cylinder:

$$\begin{aligned}\overline{\Sigma}_{rz}^{nm}(a_0,s) &= \overline{\Sigma}_{rz}^{nm}(a_{q_\mathrm{s}+q_\mathrm{c}+q_\mathrm{a}},s) = 0,\\ \overline{\Sigma}_{r\theta}^{nm}(a_0,s) &= \overline{\Sigma}_{r\theta}^{nm}(a_{q_\mathrm{s}+q_\mathrm{c}+q_\mathrm{a}},s) = 0,\end{aligned} \tag{21}_1$$

- equality of the normal stress and applied external normal load and fluid pressure at the outer/inner surfaces of the infinite cylinder:

$$\begin{aligned}\overline{\Sigma}_{rr}^{nm}(a_{q_\mathrm{s}+q_\mathrm{c}+q_\mathrm{a}},s) &= -F_{\mathrm{ex}}^{nm} - P_{nm}^{\mathrm{ex}},\\ \overline{\Sigma}_{rr}^{nm}(a_0,s) &= -F_{\mathrm{in}}^{nm} - P_{nm}^{\mathrm{in}}(a_0,s),\end{aligned} \tag{21}_2$$

- continuity of the normal fluid and solid displacements at the inner and outer surface of the infinite cylinder:

$$\begin{aligned}[Q_{nm}^{\mathrm{in}}]^{-1}P_{nm}^{\mathrm{in}}(a_0,s) &= \overline{U}_r^{nm}(a_0,s),\\ [Q_{nm}^{\mathrm{ex}}]^{-1}P_{nm}^{\mathrm{ex}}(a_{q_\mathrm{s}+q_\mathrm{c}+q_\mathrm{a}},s) &= \overline{U}_r^{nm}(a_{q_\mathrm{s}+q_\mathrm{c}+q_\mathrm{a}},s).\end{aligned} \tag{21}_3$$

2.4. Active damping and electrical boundary conditions

In this subsection, the active damping control strategy is first implemented by using a positive position feedback (PPF) controller in the first configuration, and by a positive voltage feedback controller (PVF) in the second configuration (Vel, Baillargeon, 2005). This introduces a second-order compensator forced by the radial displacement in the first configuration and the electric potential of the sensor in the second configuration both measured at the point ($z=\theta=0$), i.e.

$$\begin{aligned}\ddot{\eta}_\mathrm{p} + 2\xi_0^{\mathrm{c}1}\omega_0^{\mathrm{c}1}\dot{\eta}_\mathrm{p} + [\omega_0^{\mathrm{c}1}]^2\eta_\mathrm{p} &= [\omega_0^{\mathrm{c}1}]^2 U_r(a_{q_\mathrm{o}+q_\mathrm{a}},0,0,t),\\ \ddot{\eta}_\phi + 2\xi_0^{\mathrm{c}2}\omega_0^{\mathrm{c}2}\dot{\eta}_\phi + [\omega_0^{\mathrm{c}2}]^2\eta_\phi &= [\omega_0^{\mathrm{c}2}]^2\phi_\mathrm{s}(a_0,0,0,t),\end{aligned} \tag{22}$$

where $(\eta_\mathrm{p},\,\eta_\phi)$ are the controller coordinates, and $(\omega_0^{ci},\,\xi_0^{ci})$ $(i=1,2)$ refer to the natural frequencies and damping ratios of the controllers, respectively. Direct application of Laplace transform with respect to time (assuming zero initial conditions), keeping modal expansions (5) in mind, leads to the expression for the transformed modal controller coordinates:

$$\begin{aligned}\overline{\eta}_\mathrm{p}^{nm}(s) &= \frac{[\omega_0^{\mathrm{c}1}]^2\overline{U}_{r,nm}^{s}(a_{q_\mathrm{o}+q_\mathrm{a}},s)}{s^2+2\xi_0^{\mathrm{c}1}\omega_0^{\mathrm{c}1}s+[\omega_0^{\mathrm{c}1}]^2},\\ \overline{\eta}_\phi^{nm}(s) &= \frac{[\omega_0^{\mathrm{c}2}]^2\overline{\phi}_{nm}^{s}(a_0,s)}{s^2+2\xi_0^{\mathrm{c}2}\omega_0^{\mathrm{c}2}s+[\omega_0^{\mathrm{c}2}]^2},\end{aligned} \tag{23}$$

where $n,\ m=-\infty,\ldots,0,\ldots,+\infty$. Subsequently, the controller coordinates, magnified by positive gains, (G_p,G_ϕ) are respectively feedback as input voltages to the piezoelectric actuators in the form $\overline{\phi}_{nm}^{\mathrm{a}}(a_{q_\mathrm{o}+q_\mathrm{a}},s) = G_\mathrm{p}[\omega_0^{\mathrm{c}1}]^2\overline{\eta}_\mathrm{p}^{nm}$ in the first configuration, and $\overline{\phi}_{nm}^{\mathrm{a}}(a_{q_\mathrm{s}+q_\mathrm{o}+q_\mathrm{a}},s) = G_\phi[\omega_0^{\mathrm{c}2}]^2\overline{\eta}_\phi^{nm}$ in the second configuration.

Next, the active damping control strategy is implemented by using a negative velocity feedback (NVF) controller in the first configuration, and by a derivative voltage feedback controller (DVF) in the second configuration (Vel, Baillargeon, 2005). This introduces a second-order compensator in the form $(\theta=0,\ z=0)$, i.e.

$$\begin{aligned}\ddot{\eta}_\mathrm{v} + 2\xi_0^{\mathrm{c}1}\omega_0^{\mathrm{c}1}\dot{\eta}_\mathrm{v} + [\omega_0^{\mathrm{c}1}]^2\eta_\mathrm{v} &= [\omega_0^{\mathrm{c}1}]^2\dot{U}_r(a_{q_\mathrm{o}+q_\mathrm{a}},0,0,t),\\ \ddot{\eta}_{\dot\phi} + 2\xi_0^{\mathrm{c}2}\omega_0^{\mathrm{c}2}\dot{\eta}_{\dot\phi} + [\omega_0^{\mathrm{c}2}]^2\eta_{\dot\phi} &= [\omega_0^{\mathrm{c}2}]^2\dot{\phi}_\mathrm{s}(a_0,0,0,t),\end{aligned} \tag{24}$$

where $(\eta_\mathrm{v},\ \eta_{\dot\phi})$ denote the controller coordinates. Similarly, direct application of Laplace transform with respect to time (assuming zero initial conditions), keeping modal expansions (5) in mind, leads to the expression for the transformed modal controller coordinates:

$$\begin{aligned}\overline{\eta}_\mathrm{v}^{nm}(s) &= \frac{s[\omega_0^{\mathrm{c}1}]^2\overline{U}_{r,nm}^{s}(a_{q_\mathrm{o}+q_\mathrm{a}},s)}{s^2+2\xi_0^{\mathrm{c}1}\omega_0^{\mathrm{c}1}s+[\omega_0^{\mathrm{c}1}]^2},\\ \overline{\eta}_{\dot\phi}^{nm}(s) &= \frac{s[\omega_0^{\mathrm{c}2}]^2\overline{\phi}_{nm}^{s}t(a_0,s)}{s^2+2\xi_0^{\mathrm{c}2}\omega_0^{\mathrm{c}2}s+[\omega_0^{\mathrm{c}2}]^2},\end{aligned} \tag{25}$$

where $n,\ m=-\infty,\ldots,0,\ldots,+\infty$. Subsequently, the controller coordinates, magnified by positive gains, $(G_\mathrm{v},G_{\dot\phi})$ are respectively feedback as input voltages to the piezoelectric actuators in the form $\overline{\phi}_{nm}^{\mathrm{a}}(a_{q_\mathrm{o}+q_\mathrm{a}},s) = -G_\mathrm{v}[\omega_0^{\mathrm{c}1}]^2\overline{\eta}_\mathrm{v}^{nm}$ in the first configuration, and $\overline{\phi}_{nm}^{\mathrm{a}}(a_{q_\mathrm{s}+q_\mathrm{o}+q_\mathrm{a}},s) = G_{\dot\phi}[\omega_0^{\mathrm{c}2}]^2\overline{\eta}_{\dot\phi}^{nm}$ in the second configuration.

Now, by simple combination of the above described positive position feedback (PPF) and negative velocity feedback (NVF) controllers, the electrical boundary conditions applied onto the top and bottom surfaces of the piezoelectric actuator layer in the first configuration are written as (Vel, Baillargeon, 2005)

$$\begin{aligned}\overline{\phi}_{nm}^{\mathrm{a}}(a_{q_\mathrm{o}},s) &= 0,\\ \overline{\phi}_{nm}^{\mathrm{a}}(a_{q_\mathrm{o}+q_\mathrm{a}},s) &= (\kappa_\mathrm{p}+\kappa_\mathrm{v})\overline{U}_{r,nm}^{\mathrm{s}}(a_{q_\mathrm{o}+q_\mathrm{a}},s),\end{aligned} \tag{26}$$

where

$$\kappa_\mathrm{p} = \frac{G_\mathrm{p}[\omega_0^{\mathrm{c}1}]^4}{s^2+2\xi_0^{\mathrm{c}1}\omega_0^{\mathrm{c}1}s+[\omega_0^{\mathrm{c}1}]^2},$$

and

$$\kappa_\mathrm{v} = -\frac{G_\mathrm{v}s[\omega_0^{\mathrm{c}1}]^4}{s^2+2\xi_0^{\mathrm{c}1}\omega_0^{\mathrm{c}1}s+[\omega_0^{\mathrm{c}1}]^2}.$$

Similarly, by combining the positive voltage feedback (PVF) and derivative voltage feedback (DVF) controllers, the electrical boundary conditions applied onto the top and bottom surfaces of the piezoelectric sensor and actuator layers in the second configuration are written as (*Vel, Baillargeon*, 2005)

$$\begin{aligned}\overline{\phi}_{nm}^{\mathrm{s}}(a_{q_\mathrm{s}},s) &= \overline{D}_{r,nm}^{\mathrm{s}}(a_0,s) = 0,\\ \overline{\phi}_{nm}^{\mathrm{a}}(a_{q_\mathrm{s}+q_\mathrm{o}+q_\mathrm{a}},s) &= (\kappa_\phi+\kappa_{\dot\phi})\overline{\phi}_{nm}^{\mathrm{s}}(a_0,s),\\ \overline{\phi}_{nm}^{\mathrm{a}}(a_{q_\mathrm{s}+q_\mathrm{o}},s) &= 0,\end{aligned} \tag{27}$$

where

$$\kappa_{\phi} = \frac{G_{\phi}[\omega_0^{c2}]^4}{s^2 + 2\xi_0^{c2}\omega_0^{c2}s + [\omega_0^{c2}]^2},$$

and

$$\kappa_{\dot{\phi}} = \frac{G_{\dot{\phi}}s[\omega_0^{c2}]^4}{s^2 + 2\xi_0^{c2}\omega_0^{c2}s + [\omega_0^{c2}]^2}.$$

Lastly, by direct implementation of mechanical boundary conditions (20) and electrical boundary conditions (26) into transfer matrix relation (14), after some manipulations, one arrives at the final matrix equation for the first configuration in the form

$$\mathbf{A}_{nm}^{c1}\mathbf{x}_{nm}^{c1} = \mathbf{b}_{nm}^{c1}, \tag{28}$$

where the unknown modal coefficient vector is given by

$$\begin{aligned}\mathbf{x}_{nm}^{c1} = [&\overline{u}_r^{nm}(a_0,s),\ \overline{u}_\theta^{nm}(a_0,s),\ \overline{u}_z^{nm}(a_0,s),\\ &\overline{u}_r^{nm}(a_{q_o+q_a},s),\ \overline{u}_\theta^{nm}(a_{q_o+q_a},s),\ \overline{u}_z^{nm}(a_{q_o+q_a},s),\\ &\overline{D}_{r,nm}^{a}(a_{q_o},s),\ \overline{D}_{r,nm}^{a}(a_{q_o+q_a},s)]^{T},\end{aligned}$$

and the coefficient matrix $\mathbf{A}_{nm}^{c1}$ (8×8) and the right hand side vector $\mathbf{b}_{nm}^{c1}$ (8×1) are given in Appendix C. Anagolously, direct implementation of mechanical boundary conditions (21) and electrical boundary conditions (27) into the transfer matrix relation (16), after some manipulations, leads to the final matrix equation for the second configuration in the form

$$\mathbf{A}_{nm}^{c2}\,\mathbf{x}_{nm}^{c2} = \mathbf{b}_{nm}^{c2}\,, \tag{29}$$

where the unknown modal coefficient vector is given by

$$\begin{aligned}\mathbf{x}_{nm}^{c2} = [&\overline{U}_r^{nm}(a_0,s),\ \overline{U}_\theta^{nm}(a_0,s),\ \overline{U}_z^{nm}(a_0,s),\\ &\overline{U}_r^{nm}(a_{q_s+q_o+q_a},s),\ \overline{U}_\theta^{nm}(a_{q_s+q_o+q_a},s),\\ &\overline{U}_z^{nm}(a_{q_s+q_o+q_a},s),\ \overline{\phi}_{nm}^{s}(a_0,s),\ \overline{D}_{r,nm}^{a}(a_{q_s+q_o},s),\\ &\overline{D}_{r,nm}^{a}(a_{q_s+q_o+q_a},s),\ \overline{D}_{r,nm}^{s}(a_{q_s},s)]^{T}\end{aligned}$$

and the coefficient matrix $\mathbf{A}_{nm}^{c2}$ (10×10) and the right hand side vector $\mathbf{b}_{nm}^{c2}$ (10×1) are given in Appendix C. This ends the complete analysis of the problem. In the next section, some numerical examples are considered.

3. Numerical results

Noting the large number of parameters involved here, while keeping in view our computing hardware restrictions, specific models will be considered. Accordingly, the geometric parameters of the composite infinite cylinders, which are assumed to be filled with air ($\rho_{in} = 1.2$ kg/m^3, $c_{in} = 344.43$ m/s), and submerged in water ($\rho_{ex} = 1000$ kg/m^3, $c_{ex} = 1500$ m/s), are taken as ($a_0 = 0.492$ m, $a_{q_o} = 0.495$ m, $a_{q_o+q_a} = 0.5$ m) in the first configuration, and ($a_0 = 0.491$ m, $a_{q_s} = 0.492$ m, $a_{q_s+q_0} = 0.495$ m, $a_{q_s+q_o+q_a} = 0.5$ m) in the second configuration. The orthotropic cylindrical layers in both configurations are supposed to be made of a single layer ($q_o = 1$) of homogenous isotropic aluminum ($H_o^{c1} = H_o^{c2} = 0.003$ m, $\rho_o = 2700$ Kg/m^3, $V_o = 1$) with the material properties as provided in Table 1. The actuator/sensor layers are also assumed to be single-layered ($q_a = q_s = 1$), perfectly bonded onto the surface of the orthotropic isotropic layer ($H_a^{c1} = H_a^{c2} = 0.005$ m; $H_s^{c2} = 0.001$), made of homogenous ($V_{s,a} = 1$) PZT4 with $\rho_{s,a} = 7500$ Kg/m^3, and the mechanical and electrical material properties as given in Table 1. In all numerical simulations (except in validations), a pair of impulsive radial external loads acting at the top and bottom points ($r = 0.5$ m; $\theta = 0,\ \pi$; $z = 0$) of the hollow cylinders are considered, which can be represented by $F_{ex}(\theta,z,t) = f_0\delta(z)[\delta(\theta)+\delta(\theta-\pi)][H(t)-H(t-t_0)]$ with $f_0 = 10$ kPa and $t_0 = 5\times 10^{-5}$ sec, where $\delta(.)$ is the Dirac delta function and $H(.)$ is the Heaviside step function. Laplace transformation of the latter expression with respect to time, and subsequent application of Fourier series expansion along the axial direction (with the virtual load inter-distance parameter $L = 10$ m), leads to the transformed modal coefficient in the form:

$$F_{ex}^{nm}(s) = \frac{f_0}{2\pi Ls}(1 - e^{-t_0 s})[1 + cos(n\pi)]. \tag{30}$$

Table 1. Physical properties of the constituent materials.

		PZT4 Layer		Aluminum Layer
c_{ij}, C_{ij} (N/m^2)	C_{11}	13.9×10^{10}	c_{11}	11.234×10^{10}
	C_{12}	7.8×10^{10}	c_{12}	6.049×10^{10}
	C_{13}	7.43×10^{10}	c_{13}	6.049×10^{10}
	C_{22}	13.9×10^{10}	c_{22}	11.234×10^{10}
	C_{23}	7.43×10^{10}	c_{23}	6.049×10^{10}
	C_{33}	11.5×10^{10}	c_{33}	11.234×10^{10}
	C_{44}	2.56×10^{10}	c_{44}	2.5926×10^{10}
	C_{55}	2.56×10^{10}	c_{55}	2.5926×10^{10}
	C_{66}	3.06×10^{10}	c_{66}	2.5926×10^{10}
e_{ij} (C/m^2)	e_{15}	12.7		
	e_{24}	12.7		
	e_{31}	-5.2		
	e_{32}	-5.2		
	e_{33}	15.1		
ε_{ij} (F/m)	ε_{11}	650×10^{-11}		
	ε_{22}	650×10^{-11}		
	ε_{33}	560×10^{-11}		

A general MATLAB® code was constructed for computing the final global modal transfer matrices, $\mathbf{W}_{nm}^{c1}(s)$ (8×8) and $\mathbf{W}_{nm}^{c2}(s)$ (10×10), in Eqs. (14) and (16) for the first and second configurations respectively. Subsequently, the matrix Eqs. (28) and (29) are numerically solved for the unknown modal coefficients ($\mathbf{x}_{nm}^{c1}$, $\mathbf{x}_{nm}^{c2}$) for each index pair ($n,\ m = -\mathscr{M},\ldots,0,\ldots,+\mathscr{M}$), and the inverse Laplace trans-

forms of various field quantities are calculated by making frequent use of Durbin's numerical inversion formula (Durbin, 1973; Fan *et al.*, 2005) in the interval $[0,\ 2T_0]$ (Hasheminejad, Mousavi-akbarzadeh, 2013; Hasheminejad *et al.*, 2013):

$$\Lambda(t) = \frac{2e^{\mu t}}{T_0}\left[\frac{1}{2}\mathrm{Re}[\overline{\Lambda}t(\mu)] + \sum_{k=1}^{\widehat{N}}\left\{\mathrm{Re}\left[\overline{\Lambda}\left(\mu + \mathrm{i}k\frac{2\pi}{T_0}\right)\right]\cdot\cos\left(kt\frac{2\pi}{T_0}\right) - \mathrm{Im}\left[\overline{\Lambda}\left(\mu + \mathrm{i}k\frac{2\pi}{T_0}\right)\right]\sin\left(kt\frac{2\pi}{T_0}\right)\right\}\right], \tag{31}$$

where μ is an arbitrary real number greater than all the real parts of the singularities of $\overline{\Lambda}(s)$, $\widehat{N}$ is the truncation constant. Furthermore, to obtain stable and convergent results in all cases considered, one may select $\widehat{N} = 3500$, $\mu T_0 = 7$ with $T_0 = 2t_{\max} = 1$ s, where $t_{\max}$ is the maximum calculation time (Durbin, 1973; Su, Ma, 2012). The computations were performed in parallel on a cluster of core i7-based desktop computers, and the convergence of numerical solutions was established in a straightforward trial and error manner, i.e. by increasing the number of modes, while looking for stability in the numerical values of the calculated solutions. MATLAB Parallel Computing Toolbox (on-line document) based on multicore processors was used to accelerate the computing. The toolbox offers up to twelve MATLAB workers to execute individual loop iterations simultaneously via the "parfor-loop" command. Using a truncation constant pair of $n_{\max} = m_{\max} = \mathscr{M} = 20$ was found to lead to uniform convergence for both configurations. It is supposed that the piezo-composite cylinders do not display material damping, and the assumed damping of the hybrid laminated cylinder is a result of the feedback controllers ($\xi_0^{c1,2} = 0.15$). Also, following the controller design procedure outlined in (Vel, Baillargeon, 2005), the targeted vibration suppression of the fundamental (thickness) mode of vibration is accomplished by selecting the compensator frequencies in the first and second configurations to be approximately equal to the fundamental frequencies corresponding to the $n = 0$ circumferential modes of the composite cylinders ($\omega_0^{c1} = 2368$ rad/sec and $\omega_0^{c2} = 2329$ rad/sec), as obtained from the associated free vibration analyses (e.g. see (Chen et al., 2004)), where it should be noted that the higher order radiation modes ($n > 1$) are known to have negligible effect on sound radiation (Caresta, 2011).

Before offering the main results, the overall validity of the formulation shall be demonstrated. To do this we first computed the radial surface displacement time histories, $U_r(r = a_{q_s+q_o+q_a};\ \theta = 0, \pi/2;\ z = 0, t)$ (m), (i.e. at points $A1$ and $A2$) due to a pair of equal and opposite uniformly distributed external diametrical impulse loads acting at $(r = a_{q_s+q_o+q_a})$ over the external surface area $\left(-\frac{\pi}{4} \le \theta \le \frac{\pi}{4},\ \frac{3\pi}{4} \le \theta \le \frac{5\pi}{4};\ -1 \le z \le 1\ \mathrm{m};\ d_{ex} = 2\ \mathrm{m}\right)$ of a piezocomposite (short-circuited) tri-laminate (PZT4/Al/PZT4) air-filled water-submerged hollow cylinder ($a_0 = 0.3$ m, $a_{q_s} = 0.4$ m, $a_{q_s+q_o} = 0.5$ m, $a_{q_s+q_o+q_a} = 0.6$ m; $\overline{\phi}_s(r = a_0,\ a_{q_s};\ \theta, z, s) = 0$, $\overline{\phi}_a(r = a_{q_s+q_o},\ a_{q_s+q_o+q_a};\ \theta, z, s) = 0$), represented by

$$F_{ex}(\theta, z, t) = f_0\left[H\left(\theta + \frac{\pi}{4}\right) - H\left(\theta - \frac{\pi}{4}\right) + H\left(\theta - \frac{3\pi}{4}\right) - H\left(\theta - \frac{5\pi}{4}\right)\right]\cdot[H(z+1) - H(z-1)][H(t) - H(t-t_0)]$$

with $f_0 = 1$ MPa and $t_0 = 5 \times 10^{-4}$ sec. Laplace transformation of the latter expression with respect to time, and subsequent application of Fourier series expansion along the axial direction, leads to the transformed modal coefficient in the form:

$$F_{nm}^{ex}(s) = (f_0\Omega_n\Gamma_m/s)(1 - \mathrm{e}^{-t_0 s}),$$

where

$$\Omega_n = \begin{cases} 1/2 & (n = 0), \\ [1+(-1)^n](\mathrm{e}^{\mathrm{i}n\pi/4} - \mathrm{e}^{-\mathrm{i}n\pi/4})/(2n\pi\mathrm{i}) & (n \ne 0), \end{cases} \tag{32}$$

$$\Gamma_m = \begin{cases} 4/L & (m = 0), \\ \sin(4m\pi/L)/(m\pi) & (m \ne 0). \end{cases}$$

Very good agreements are obtained with the results calculated by using the commercial finite element code ABAQUS (on-line documentation), as shown in Fig. 2a. Also shown in the same figure are the good agreements obtained for the calculated radiated acoustic pressure time response, $p_{ex}(r = a_{q_s+q_o+q_a},\ 2a_{q_s+q_o};\ \theta = 0;\ z = 0;\ t)$, at the selected positions ($A1$, $A3$). In the ABAQUS model, a very long piezo-composite hollow cylinder of 200 m length was used in order to properly capture the transient wave interaction effects before the reflection of the structure-borne waves from the truncated ends of the cylinder. Furthermore, the nonreflecting acoustic boundary condition was adopted far enough (about 40 m) away from the submerged cylinder so that the approximation of normally impinging sound waves was sufficiently accurate, with little reflection of outgoing sound energy back into the surrounding acoustic medium. Moreover, about 11700 C3D20RE (20-node quadratic piezoelectric brick reduced integration) elements were used to model the PZT4 actuator/sensor layers, and about 6000 C3D20R (20-node quadratic brick reduced integration) elements were used to model the aluminum core layer in the ABAQUS model. Also, about 75000 AC3D20 (20-node quadratic acoustic brick) elements were employed to model the internal and external acoustic fluids. In addition, mesh size sensitivity analysis was carried out for numerical convergence checking.

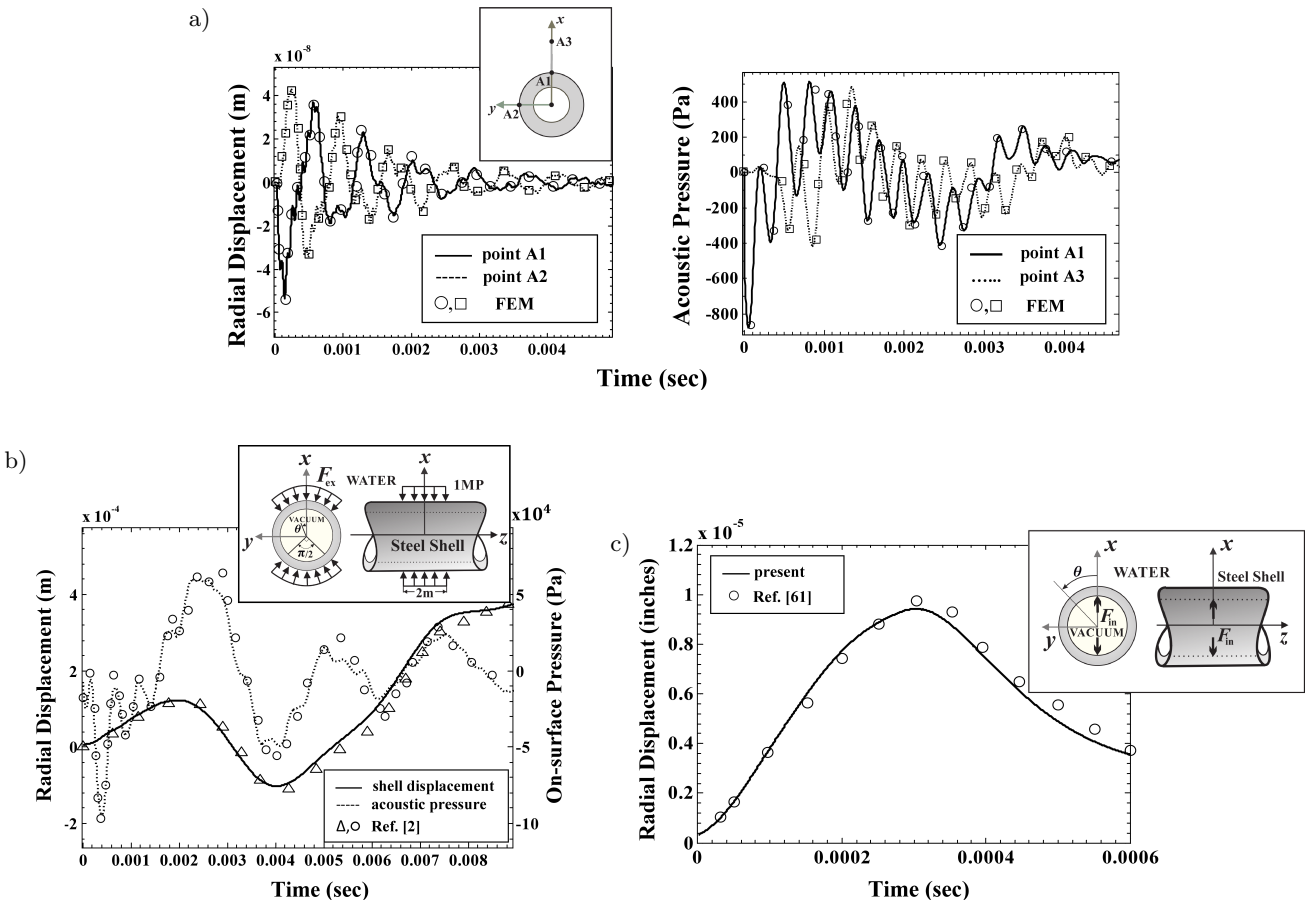

Fig. 2. a) Radial surface displacement and radiated acoustic pressure time histories due to a pair of equal and opposite uniformly distributed external diametrical impulse loads for a tri-laminate (PZT4/Al/PZT4) air-filled/water-submerged piezocomposite hollow cylinder. b) Radial surface displacement and on-surface pressure response due to a pair of equal and opposite uniformly distributed radial impulsive external loads for an evacuated water-submerged thin steel cylindrical shell. c) Radial surface displacement response due to a pair of impulsive radial internal loads for an evacuated water-submerged thin steel cylindrical shell.

As a further attempt to check the validity of our structural formulation, we set the thicknesses of the external PZT4 actuator and Aluminum core layers nearly equal to zero in our general Matlab code (e.g., $H_{\rm o} = H_{\rm a} = 0.000001$ m), and used it to compute the time-domain radial displacement response, $U_r(r = a_{q_{\rm s}};\, \theta = z = 0,\, t)$, of a single-layer inactive (short circuited) FGPM (PZT4) cylinder ($V_{\rm s} = 1$; $q_{\rm s} = 10$; $a_0 = 1$ m; $a_{q_{\rm s}} = 1.05$ m; $\overline{\phi}_{\rm s}(r = a_0, a_{q_{\rm s}};\, \theta, z, s) = 0$), in the absence of internal and external fluids ($\rho_{\rm ex} = \rho_{\rm in} = 0$) under the action of a pair of constant amplitude radial impulsive point loads represented by

$$F_{\rm ex}(\theta, z, t) = f_0 \delta(z)[\delta(\theta) + \delta(\theta - \pi)]\delta(t)$$

with $f_0 = 1$ MPa. Laplace transformation of the latter expression with respect to time, and subsequent application of Fourier series expansion along the axial direction, leads to the transformed modal coefficient in the form

$$F_{\rm ex}^{nm}(s) = \frac{f_0}{2\pi L}[1 + \cos(n\pi)].$$

Afterward, we applied the standard Fast Fourier Transform (FFT) to the calculated time-domain radial displacement response to arrive at the associated frequency response function. Table 2 indicates the good agreements attained between the calculated the lowest natural (peak resonant) frequencies ($\omega a_0 \sqrt{\rho_{\rm s}/C_{44}}$) of the infinite PZT-4 hollow cylinder with the data presented in Table 1 of (Ding *et al.*, 1997; Chen *et al.*, 2004).

Next, we set the thicknesses of the piezoelectric layers in the second configuration nearly equal to zero and used our general code to compute the radial displacement response, $U_r(a_{q_{\rm s}+q_{\rm o}+q_{\rm a}} = 1.0001$ m, $\theta = \pi/2, z = 0, t)$, as well as the on-surface acoustic pressure, $p_{\rm ex}(a_{q_{\rm s}+q_{\rm o}+q_{\rm a}} = 1.0001$ m, $\theta = \pi/2$, $z = 0$, $t)$, due to a pair of equal and opposite uniformly distributed external diametrical impulse loads acting at ($r = a_{q_{\rm s}+q_{\rm o}+q_{\rm a}} = 1.0001$ m) over the external surface area $\left(-\frac{\pi}{4} \le \theta \le \frac{\pi}{4}, \frac{3\pi}{4} \le \theta \le \frac{5\pi}{4}; -1 \le z \le 1 \text{ m}; d_{\rm ex} = 2 \text{ m}\right)$ of an evacuated water-submerged cylindrical shell

Table 2. Comparison of the calculated lowest natural frequencies of an infinite PZT-4 hollow cylinder with the data presented in (Ding *et al.*, 1997; Chen *et al.*, 2004).

	$\chi = 0.500$				$\chi = 1.000$			
	$n=0$	$n=1$	$n=2$	$n=3$	$n=0$	$n=1$	$n=2$	$n=3$
Ding *et al.*, 1997	1.43728	0.69679	1.29820	2.23647	2.07361	1.65614	1.90402	2.84573
Chen *et al.*, 2004	1.44270	0.69744	1.24537	–	2.07745	1.65696	1.90435	–
present	1.48694	0.67221	1.29330	2.26265	2.09246	1.64250	1.90939	2.89349

as represented in Eq. (31), with $f_0 = 1$ MPa and $t_0 = 5 \times 10^{-4}$ sec, and

$$F_{nm}^{\mathrm{ex}}(s) = (f_0 \Omega_n \Gamma_m / s)(1 - \mathrm{e}^{-t_0 s}).$$

Figure 2b illustrates the good agreements obtained with the results presented in Fig. 3b of (Hasheminejad, Mousavi-akbarzadeh, 2013), which are based on Donnell's thin shell theory.

As a final check, we set the thicknesses of the piezoelectric layers in the second configuration nearly equal to zero and calculated the radial displacement response, $U_r(a_{q_\mathrm{s}+q_\mathrm{o}+q_\mathrm{a}} = 20.50001\,\mathrm{inches}, \theta = 0, z = 0, t)$, due to a pair of impulsive radial loads acting at the top and bottom points on the internal surface of an evacuated water-submerged cylindrical shell ($r = a_0 = 19.4999\,\mathrm{inches}; \theta = 0, \pi; z = 0$) with ($a_{q_\mathrm{s}} = 19.5$, $a_{q_\mathrm{s}+q_\mathrm{o}} = 20.5$ inches) represented by

$$F_{\mathrm{in}}(\theta, z, t) = f_0 \delta(z)[\delta(\theta) + \delta(\theta - \pi)][H(t) - H(t - t_0)]$$

with $f_0 = 1$ Psi and $t_0 = 3 \times 10^{-4}$ sec. Laplace transformation of the latter expression with respect to time, and subsequent application of Fourier series expansion along the axial direction, leads to the transformed modal coefficient in the form:

$$F_{\mathrm{in}}^{nm}(s) = \frac{f_0}{2\pi L s}(1 - \mathrm{e}^{-t_0 s})[1 + \cos(n\pi)].$$

The outcome, as shown in Fig. 2c, shows good agreement with that presented in Fig. 8 of (Wang, Berger, 1971).

In this work, the simple trial and error approach is avoided and the Genetic Algorithm build in Matlab Global Optimization Toolbox (Ref. 21) is utilized to efficiently identify and optimize the controller parameters. The GA optimization process tracks the following general steps: generate a random initial population of parents or potential solutions, evaluate the fitness of every parent in the population, apply selection, crossover and mutation and substitute the actual population with the new population. Over consecutive generations, the population progresses toward an optimal solution and the algorithm halt when the stopping criterion is achieved. The optimized model considered here is a multi-objective design problem, where the primary fitness or objective functions, which account for evaluation of the solution at each step, are selected as the controlled radiated acoustic pressure, cylinder radial surface displacement, and actuator voltage. In particular, for simultaneous tuning of the controller gain parameters (G_p, G_ϕ) and $(G_\mathrm{v}, G_{\dot{\phi}})$, genetic algorithm may be applied to minimize the following cost function (Bélanger, 1995):

$$\begin{aligned} J = \min \int_0^{t_{\max}} \Big\{ & Q_p [p_{\mathrm{ex}} / \max(p_{\mathrm{ex}}^{\mathrm{uncont}})]^2 \\ & + Q_{U_r} [U_r / \max(U_r^{\mathrm{uncont}})]^2 \\ & + R_\phi [\phi_\mathrm{a} / \max(\phi_\mathrm{a}^{\mathrm{uncont}})]^2 \Big\} \, \mathrm{d}t, \end{aligned} \tag{33}$$

where each parameter is normalized with respect to the corresponding maximum calculated value of the uncontrolled problem. As the control performance depends on the choices of the weight functions (Q_p, Q_{U_r}, R_ϕ), the relative magnitudes of weighting functions are selected to compromise the requirements on minimizing system elasto-acoustic energy against control voltage. A larger R_ϕ sets higher demand on control voltage, while a larger (Q_p, Q_{U_r}) further bounds the system elasto-acoustic energy. Once the weighting functions associated with system elasto-acoustic energy and control voltage are selected, then the remaining procedure is a standard optimization algorithm carried out through the Matlab GA Toolbox. Table 3 displays the configuration used in the adopted GA optimization procedure. Three distinct weight combinations are considered in the present study. In the first case, maximum

Table 3. The configuration used in the GA-optimization procedure.

Population type	double vector	Mutation function	uniform
Population size	15	Stall generations	50
Generations	50	Function tolerance	1e-6
Elite count	2	Migration Direction	forward
Crossover fraction	0.8	Migration Fraction	0.2
Creation function	uniform	Migration Interval	20
Selection function	stochastic	Initial penalty	10
Crossover function	scattered	Penalty factor	100

weight is given to the radiated acoustic pressure calculated at the near-field point $A3$, i.e. $p_{\rm ex}(r = 2a_{q_{\rm s}+q_{\rm o}} = 1\ {\rm m};\ \theta = 0;\ z = 0;\ t)$, by setting ($Q_p = 500$, $Q_{U_r} = 0$, $R_\phi = 1$). In the second case, maximum weight is given to the radial surface displacement calculated at point $A1$, i.e. $U_r(r = a_{q_{\rm s}+q_{\rm o}+q_{\rm a}} = 0.5\ {\rm m};\ \theta = 0;\ z = 0,\ t)$, by setting ($Q_p = 0$, $Q_{U_r} = 500$, $R_\phi = 1$). In the third case, maximum weight is given to the actuator voltage signal calculated at point $A1$, i.e. $\phi_{\rm a}(r = 0.5\ {\rm m};\ \theta = 0;\ z = 0,\ t)$, by setting ($Q_p = 1$, $Q_{U_r} = 1$, $R_\phi = 500$). Here it should be noted that the actuator weight function R_ϕ is never identically set equal to zero, as the control effect must be considered in all cost functions. When either of the maximum generation number, stall generation, or function tolerance has been reached (see Table 3), the GA-based optimization process terminates, and the best control parameters are accordingly applied for control.

Figure 3a displays the uncontrolled and controlled radiated acoustic near-field pressure time histories, $p_{\rm ex}(r = 1\ {\rm m};\ \theta = z = 0;\ t)$, calculated at point $A3$, for the smart cylinders subjected to the impulsive pair of diametrical external point loads ($f_0 = 10$ kPa, $t_0 = 5 \times 10^{-5}$ sec), in two basic control configurations, and for the three weighting parameter combinations describe above. Figure 3b shows the uncontrolled and controlled radiated acoustic center-point pressure time histories, $p_{\rm in}(r = 0;\ \theta = z = 0;\ t)$ calculated at point O for the two control configurations and the three weighting parameter combinations. Also, Figs. 3c and 3d respectively display the corresponding radial surface displacement responses, $U_r(r = 0.5\ {\rm m};\ \theta = z = 0;\ t)$ and the applied actuator voltage time histories, $\phi_{\rm a}(r = 0.5\ {\rm m};\ \theta = z = 0;\ t)$, both calculated at point $A1$, for the selected control configurations and weighting parameters. Here, it should be noted that in the transient structure/fluid interaction problems, it is very common to apply a pair of equal and opposite impulsive diametrical point loads, in order to exclude the rigid body motion in the solution and avoid acceleration of the freely suspended (submerged) structure (e.g., see (Hasheminejad *et al.*, 2011; Hasheminejad, Mousavi-akbarzadeh, 2013; 2015; Wang, Berger, 1971).) Furthermore, as noted earlier, Matlab's GA Toolbox is used to simultaneously tune the controller gain parameters ($G_{\rm p}, G_{\rm v}$) in the first configuration, and the gain parameters ($G_\phi, G_{\dot\phi}$) in the second configuration. The most important observations are as follows. Examination of the four subplots in the first and second rows of the figure indicates that the best control action for the acoustic pressure in both control configurations generally occurs in the first weighting combination ($Q_p = 500$, $Q_{U_r} = 0$, $R_\phi = 1$), where the maximum weight in the cost function (33) is given to $p_{\rm ex}(r = 1\ {\rm m};\ \theta = z = 0;\ t)$ (i.e. note the substantially restrained pressure curve oscillations signified by the red lines in all four subplots). Similarly, simple inspection of the two subplots in the third row of the figure shows that the best control action for the radial cylinder surface displacement in both control configurations happens in the second weighting combination ($Q_p = 0$, $Q_{U_r} = 500$, $R_\phi = 1$), where the maximum weight in the cost function (33) is given to $U_r(r = 0.5\ {\rm m};\ \theta = 0;\ z = 0;\ t)$ (i.e. note the significantly controlled displacement curve oscillations signified by the green lines in both subplots). Also, simple checking of the two subplots in the last row of the figure demonstrates that the best control action with a minimum applied actuator voltage constraint occurs in the third weighting combination ($Q_p = 1$, $Q_{U_r} = 1$, $R_\phi = 500$), where the maximum weight in the cost function (33) is given to $\phi_{\rm a}(r = 0.5\ {\rm m};\ \theta = 0;\ z = 0;\ t)$ (i.e. note the significantly controlled actuator voltage curve oscillations indicated by the blue lines in both subplots). The above remarks naturally very well follow the physics of the control problem and were largely expected. The most interesting observation is perhaps the fact that the ADC control actions in the first control configuration (i.e. the PPF/NVF controllers appearing in the 1st column subplots) are in general superior to those of the second control configuration (i.e. the PVF/DVF controllers in the second column subplots), at the expense of higher overall applied voltages especially at the very beginning of control action ($t < 0.01$ sec). In particular, the very best control action is observed through substantial suppression of the cylinder radial surface displacement amplitude $U_r(r = 0.5\ {\rm m};\ \theta = 0;\ z = 0;\ t)$ in the second weighting combination ($Q_p = 0$, $Q_{U_r} = 500$, $R_\phi = 1$) (i.e. note the significantly reduced surface displacement amplitudes indicated by the green curve in the first subplot of the third row). Moreover, one can conclude that when adopting the ADC control strategy in transient fluid/structure interaction problems, the first control (PPF/NVF) configuration may be employed if the primary goal of control action is to substantially suppress the structural motion, while the second control (PVF/DVF) configuration may be utilized if the principal aim is to suppress the radiated pressure, keeping in mind the moderately lower applied control effort in the latter configuration. Lastly, Table 4 presents the numerical values of the maximum applied actuator voltage signal magnitudes, $|\phi_{\rm a}^{\rm max}(r = 0.5\ {\rm m};\ \theta = 0;\ z = 0;\ t)|$, calculated at the measurement point $A1$, for the selected control configurations and weighting parameters (note that vertical scales in Fig. 3d are magnified in order to improve clarity) Here, noting the moderately large thickness of the adopted PZT4 actuator layers in both control configurations ($H_{\rm a}^{\rm c1} = H_{\rm a}^{\rm c2} = 0.005$ m), and keeping in mind that the maximum allowable voltage magnitude for the selected piezo-ceramic material is normally in the range $500 \le |\phi_{\rm a}^{\rm max}| \le 1000$ V/mm (Morgan Matroc Incorporated, 1993; Bruch *et al.*,

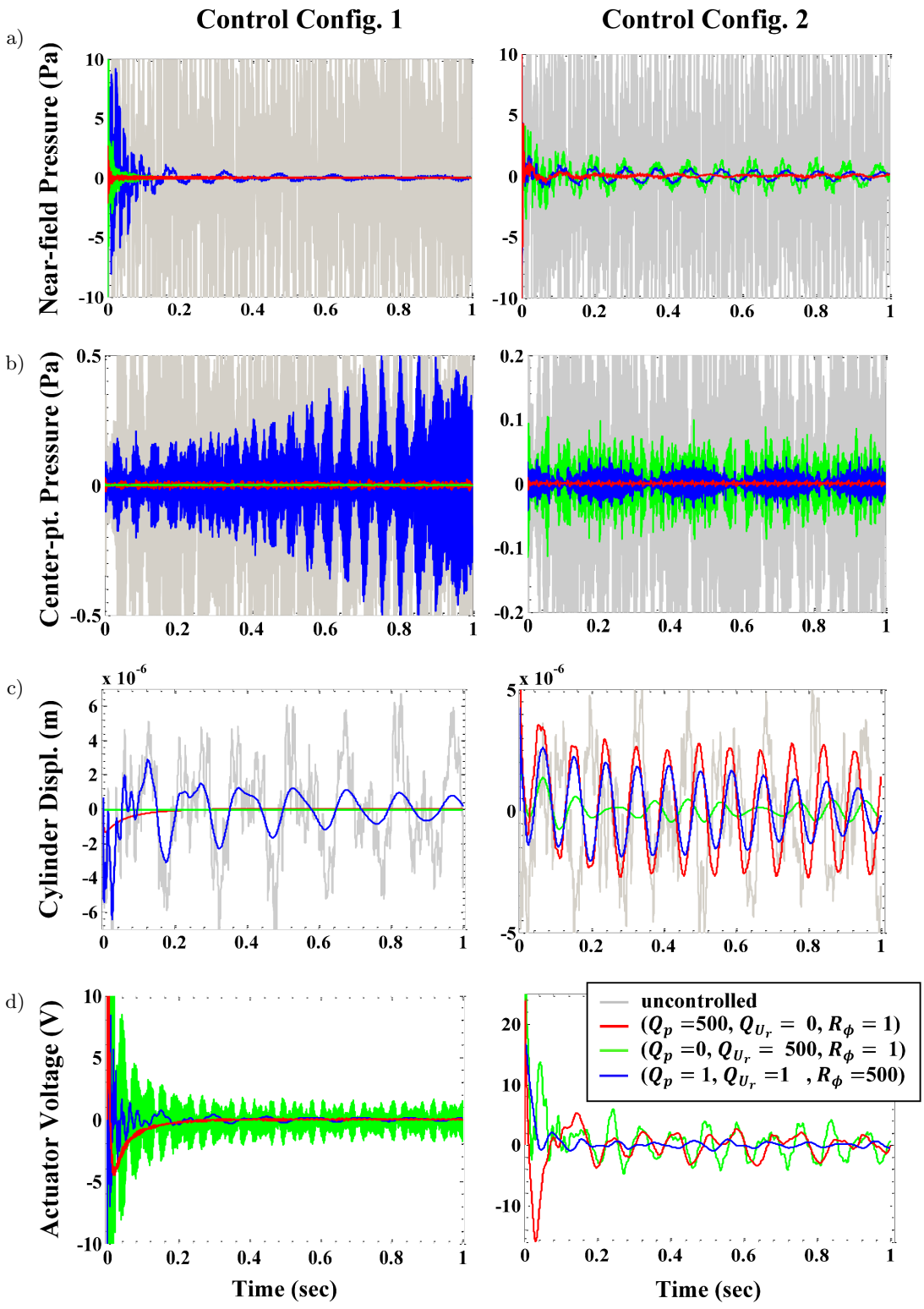

Fig. 3. a) Effect of control action on the radiated acoustic near-field pressure time history, $p_{\mathrm{ex}}(r=1,\theta=z=0,t)$, of the smart cylinder under the action of an impulsive pair of diametrical external point loads for two basic control configurations and selected weighting parameters. b) Effect of control action on the radiated acoustic internal center-point pressure time history, $p_{\mathrm{in}}(r=0,\theta=z=0,t)$ of the smart cylinder under the action of an impulsive pair of diametrical external point loads for two basic control configurations and selected weighting parameters. c) Effect of control action on the radial surface displacement response, $U_r(r=0.5\ \mathrm{m},\theta=z=0,t)$ of the smart cylinder under the action of an impulsive pair of diametrical external point loads for two basic control configurations and selected weighting parameters. d) Applied actuator voltage time history, $\phi_{\mathrm{a}}(r=0.5\ \mathrm{m},\theta=z=0,t)$, of the smart cylinder for two basic control configurations and selected weighting parameters.

2000), a simple comparison with the largest calculated control voltage magnitude listed in Table 4 (i.e. $|\phi_{\rm a}^{\rm max}| = 177$ V/mm) clearly demonstrates that the applied control voltages are far below the overload limit of the piezo-ceramic actuator layer in both control configurations.

Table 4. Maximum calculated applied actuator voltage magnitudes, $|\phi_{\rm a}^{\rm max}(r = 0.5\ {\rm m}, \theta = 0, z = 0, t)|$, in Fig. 3d, for selected control configurations and weighting parameters.

Weighting parameters	Maximum control voltage magnitude, $\lvert\phi_{\rm a}^{\rm max}\rvert$ (Volt)	
	Config. 1	Config. 2
$Q_p = 500$, $Q_{U_r} = 0$, $R_\phi = 1$	95.12	23.86
$Q_p = 0$, $Q_{U_r} = 500$, $R_\phi = 1$	**177.00**	81.04
$Q_p = 1$, $Q_{U_r} = 1$, $R_\phi = 500$	17.36	16.63

Figure 4a displays the series of selected two-dimensional time-domain snapshots ($0.1 \leq t \leq 0.7$ ms) of the uncontrolled and GA-optimized controlled internal/external radiated acoustic pressure fields along two selected cross sections of the piezocomposite cylinder (i.e. "Section A" and "Section B" being one diameter away, as marked in the last row of the figure), subjected to the impulsive pair of radial external loads, for the first weighting parameter combination ($Q_p = 500$, $Q_{U_r} = 0$, $R_\phi = 1$) in the second control configuration (G_ϕ, $G_{\dot\phi}$). Also, Fig. 4b shows the time-domain snapshots ($0.9 \leq t \leq 2.3$ ms) of only the uncontrolled internal/external radiated sound fields along the two selected cross sections of the piezocomposite cylinder in the second configuration. The associated GA-optimized (controlled) pressure snapshots are not displayed, as the perturbed pressure fields are apparently negligible in late-time ($t > 0.9$ ms). The most important observations are as follows. First, we shall consider the uncontrolled situation (i.e. the first three columns in the figure). At the very beginning of interaction, immediately following the application of the impulsive load pair, elastic waves are induced within the piezocomposite cylinder that propagate around it, superpose, and propagate back to the apex points. This elastic process is in consort with continuous radiation of acoustic waves into the surrounding fluid mediums, where dispersive structure-borne helical waves, spreading in two opposite directions in a spiral fashion, are formed around and along the cylinder, with the corresponding radial cylinder displacements producing leaky bulk waves that take energy away from the structure (Hasheminejad, Mousavi-akbarzadeh, 2012; Hanarvar *et al.*, 2011; Überall, 2001). In particular, the negative amplitude shell-induced circumnavigating waves propagating ahead of the primary (positive amplitude) propagating sound wave front are formed (e.g. note the blue-colored spherical wave fronts travelling in opposite directions ahead of the red coloured wave fronts in the external fluid which are induced by the "piston-like" motion of the cylinder at the apex points, as seen in the $t = 0.3{-}0.7$ ms A-section snapshots (Hasheminejad, Mousavi-akbarzadeh, 2013)). These waves are primarily provoked by the relatively high-magnitude compression/tension developed within the shell wall due to its inward/outward motions immediately following the application of the impulsive load pair in early times. Formation of such negative amplitude shell-induced pressure waves may result in separation of the shell from the external fluid in a real physical situation, increasing the prospect of cavitation. A similar phenomenon can be observed in the internal fluid space. In particular, the shell-induced pair of internal (blue colored) wave fronts which propagate in opposite directions along the x-axis as well as the primary propagation (red colored) wave fronts consecutively collide and substantially amplify each other exactly at the centre of the cylindrical cavity in moderate-times ($t = 1.5$ ms) (see Fig. 4b). From then on (i.e. after the two wave fronts pass through each other), the entire acoustic domain inside the cylindrical space gets fully involved. During the any of these stages ($t \geq 1.7$ ms), several low/high amplitude pressure spots are formed that could be related to radiation of the shell-induced circumnavigating waves into the internal fluid associated with various structural vibration modes. In later times, the higher order vibrations modes get involved, the internal acoustic energy redistributes, and the pressure spots linked to different vibration modes get more complicated with lower amplitudes. The transient developments in the B-section are very similar to those of the A-section, expect that they are of substantially lower amplitudes, and there are time delays owing to the spherical geometry of the propagating wave fronts along the cylinder axis. In the controlled problem (i.e. the last three columns in the Fig. 4a), a similar situation in regard to formation and propagation of primary (positive amplitude) and shell-induced (negative amplitude) waves in the internal and external acoustic fluid mediums is observed. The main distinction here is the noticeable (remarkable) reduction in the amplitude of the sound waves radiated outward (inward) into the surrounding (internal) fluid medium. In particular, the very high efficiency of the adopted control system in nearly complete annihilation (good attenuation) of the internal (external) acoustic field immediately following the application of the impulsive load pair in early times could be directly linked to the distributed nature of the piezoelectric sensor/actuator layers in the context of the active damping control strategy. More detailed comparisons of the uncontrolled and controlled transient sound fields can be observed by execution of a recently posted animation clip (http://www.mediafire.com).

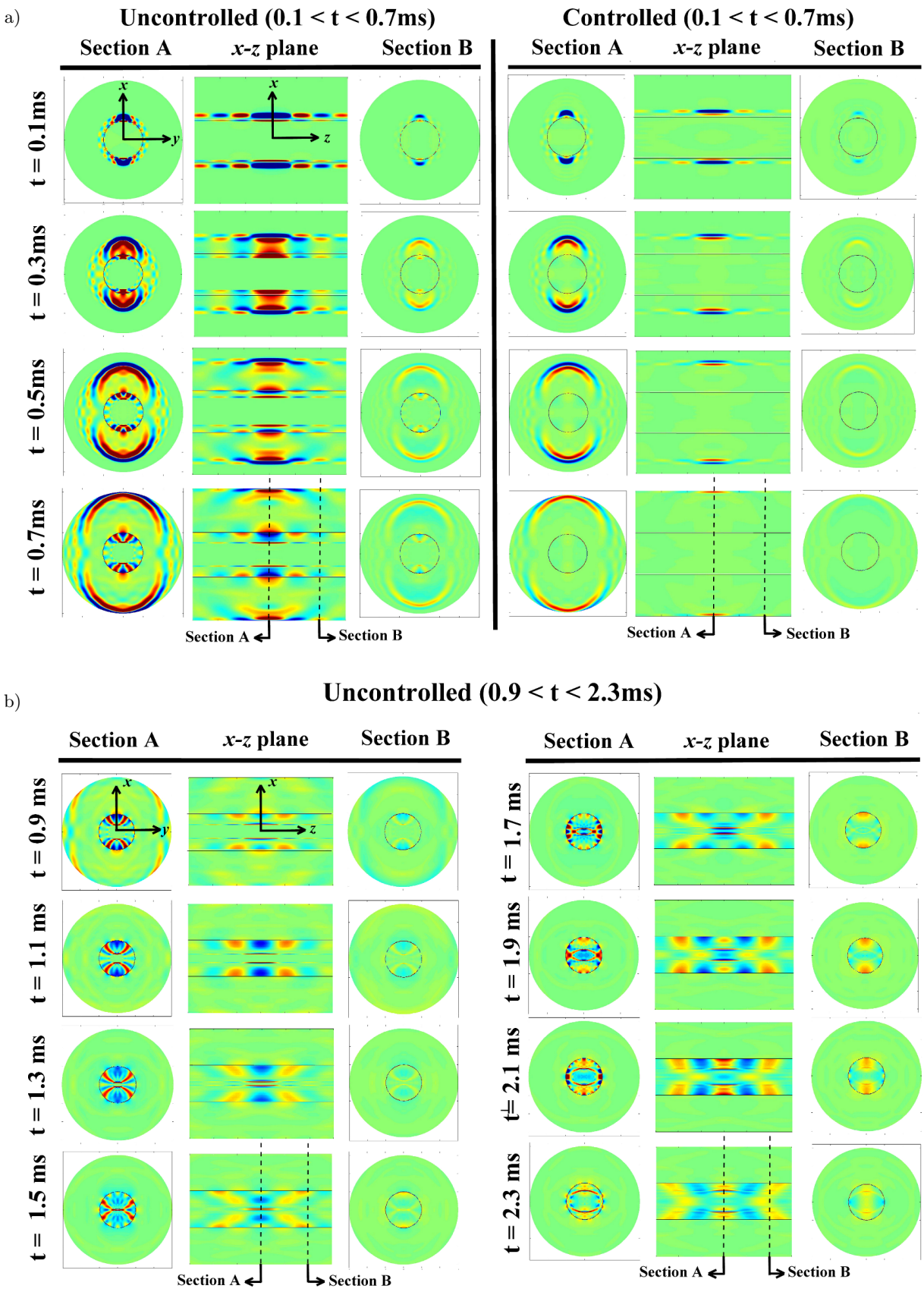

Fig. 4. a) Effect of control action on the early-time internal/external sound pressure fields due to an impulsive pair of diametrical external point loads acting on the smart cylinder in the second control configuration (Config. 2). b) Moderate to late-time images of the internal/external sound pressure fields for the uncontrolled three-layered piezo-composite cylinder (Config. 2).

4. Conclusions

Transient three-dimensional acoustic radiation control of an infinitely-long hollow piezolaminated cylinder under general time-dependent distributed electromechanical excitations has been performed using the active damping control (ADC) strategy in two basic configurations. The fully coupled elasto-acoustic system is analyzed by employing the spatial state-space model based on the exact piezo-elasticity theory, while the ADC strategy is built on the PPF/NVF and PVF/DVF control laws in the first and second configurations, respectively. The Matlab Genetic Algorithm (GA) Toolbox is utilized for tuning the control gain parameters with a multi-objective cost function involving appropriate weight functions. Also, Matlab Parallel Computing Toolbox (PCT) based on multicore processors is used to accelerate the computing. Time response histories and snapshots (animations) for a pair of equal and opposite impulsive external point excitations are presented and discussed. The most important observations are summarized as follows.

The best control action for the radiated sound fields (radial cylinder surface displacement) in both control configurations is observed for the first (second) weighting combination, where the maximum weight is given to the external near-field acoustic pressure (radial surface displacement), with the actuator voltage being well within the acceptable range. Similarly, a moderate sound attenuation with a minimum control effort occurs for the third weighting combination, where the maximum weight is given to the actuator voltage itself. Also, the ADC control performance in the first control configuration is found to be superior to that of the second configuration, at the expense of a higher overall applied voltage, especially at the very beginning of control action. Furthermore, it is suggested that the first control (PPF/NVF) configuration could be employed if the primary goal of control action is to substantially dampen the structural motion, while the second control (PVF/DVF) configuration may be utilized if the principal aim is to suppress the radiated pressure, keeping in mind the notably lower initially applied control effort in the latter configuration.

At the very beginning of interactions in the uncontrolled situation, mainly due to the "piston-like" motion of the cylinder wall, acoustic waves are continuously radiated, and the negative amplitude shell-induced circumnavigating waves propagate in the external fluid ahead of the positive amplitude primary sound waves. A similar phenomenon is observed in the internal fluid space at moderate-times, where the shell-induced waves in company with primary propagating waves travel in opposite directions, consecutively colliding at the centre of the cylindrical cavity, and substantially amplifying each other. From then on, acoustic energy inside the cylindrical space redistributes, the entire fluid domain gets fully involved, and several low/high amplitude pressure spots are formed linked to radiation of the shell-induced circumnavigating waves. In the controlled problem, on the other hand, there is a noticeable (remarkable) reduction in the amplitude of the sound waves radiated outward (inward) into the surrounding (internal) fluid medium. In particular, the very high efficiency of the adopted control system in nearly complete annihilation (good attenuation) of the internal (external) acoustic field immediately following the application of the impulsive load pair in early times is directly linked to the distributed nature of the piezoelectric sensor/actuator layers in context of the active damping control strategy.

Appendix A

$$\mathbf{c} = \begin{bmatrix} c_{11} & c_{12} & c_{13} & 0 & 0 & 0 \\ c_{12} & c_{22} & c_{23} & 0 & 0 & 0 \\ c_{13} & c_{23} & c_{33} & 0 & 0 & 0 \\ 0 & 0 & 0 & c_{44} & 0 & 0 \\ 0 & 0 & 0 & 0 & c_{55} & 0 \\ 0 & 0 & 0 & 0 & 0 & c_{66} \end{bmatrix},$$

$$\mathbf{C} = \begin{bmatrix} C_{11} & C_{12} & C_{13} & 0 & 0 & 0 \\ C_{12} & C_{22} & C_{23} & 0 & 0 & 0 \\ C_{13} & C_{23} & C_{33} & 0 & 0 & 0 \\ 0 & 0 & 0 & C_{44} & 0 & 0 \\ 0 & 0 & 0 & 0 & C_{55} & 0 \\ 0 & 0 & 0 & 0 & 0 & C_{66} \end{bmatrix},$$

$$\mathbf{e} = \begin{bmatrix} e_{11} & e_{21} & e_{31} \\ e_{12} & e_{22} & e_{32} \\ e_{13} & e_{23} & e_{33} \\ e_{14} & e_{24} & e_{34} \\ e_{15} & e_{25} & e_{35} \\ e_{16} & e_{26} & e_{36} \end{bmatrix},$$

$$\mathbf{K} = \begin{bmatrix} \frac{1}{r} & \frac{1}{r}\frac{\partial}{\partial\theta} & 0 \\ 0 & 0 & \frac{\partial}{\partial z} \\ \frac{\partial}{\partial r} & 0 & 0 \\ \frac{1}{2}\frac{\partial}{\partial z} & 0 & \frac{1}{2}\frac{\partial}{\partial r} \\ \frac{1}{2r}\frac{\partial}{\partial\theta} & \frac{1}{2}\frac{\partial}{\partial r} - \frac{1}{2r} & 0 \\ 0 & \frac{1}{2}\frac{\partial}{\partial z} & \frac{1}{2r}\frac{\partial}{\partial\theta} \end{bmatrix},$$

$$\mathbf{p} = \begin{bmatrix} 0 & 0 & \dfrac{\partial}{\partial r}+\dfrac{1}{r} & \dfrac{\partial}{\partial z} & \dfrac{1}{r}\dfrac{\partial}{\partial \theta}-\dfrac{1}{r} & 0 \\ \dfrac{1}{r}\dfrac{\partial}{\partial \theta} & 0 & 0 & 0 & \dfrac{\partial}{\partial r}+\dfrac{2}{r} & \dfrac{\partial}{\partial z} \\ 0 & \dfrac{\partial}{\partial z} & 0 & \dfrac{\partial}{\partial r}+\dfrac{1}{r} & 0 & \dfrac{1}{r}\dfrac{\partial}{\partial \theta} \end{bmatrix},$$

$$\mathbf{P} = \begin{bmatrix} 0 & 0 & \dfrac{\partial}{\partial r}+\dfrac{1}{r} & \dfrac{\partial}{\partial z} & \dfrac{1}{r}\dfrac{\partial}{\partial \theta}-\dfrac{1}{r} & 0 & 0 & 0 & 0 \\ \dfrac{1}{r}\dfrac{\partial}{\partial \theta} & 0 & 0 & 0 & \dfrac{\partial}{\partial r}+\dfrac{2}{r} & \dfrac{\partial}{\partial z} & 0 & 0 & 0 \\ 0 & \dfrac{\partial}{\partial z} & 0 & \dfrac{\partial}{\partial r}+\dfrac{1}{r} & 0 & \dfrac{1}{r}\dfrac{\partial}{\partial \theta} & 0 & 0 & 0 \\ 0 & 0 & 0 & 0 & 0 & 0 & \dfrac{\partial}{\partial r}+\dfrac{1}{r} & \dfrac{1}{r}\dfrac{\partial}{\partial \theta} & \dfrac{\partial}{\partial z} \end{bmatrix},$$

$$\boldsymbol{\varepsilon} = \begin{bmatrix} \varepsilon_{11} & 0 & 0 \\ 0 & \varepsilon_{22} & 0 \\ 0 & 0 & \varepsilon_{33} \end{bmatrix}.$$

Appendix B

$$\mathbf{g}_{nm}(r,s) = \begin{bmatrix} \mathbf{g}_{nm}^{(1,1)} & \mathbf{g}_{nm}^{(1,2)} \\ \mathbf{g}_{nm}^{(2,1)} & \mathbf{g}_{nm}^{(2,2)} \end{bmatrix}, \qquad \mathbf{G}_{nm}(r,s) = \begin{bmatrix} \mathbf{G}_{nm}^{(1,1)} & \mathbf{G}_{nm}^{(1,2)} & \mathbf{G}_{nm}^{(1,3)} & \mathbf{G}_{nm}^{(1,4)} \\ \mathbf{G}_{nm}^{(2,1)} & \mathbf{G}_{nm}^{(2,2)} & \mathbf{G}_{nm}^{(2,3)} & \mathbf{G}_{nm}^{(2,4)} \end{bmatrix},$$

where

$$\mathbf{g}_{nm}^{(1,1)} = \begin{bmatrix} -\dfrac{c_{13}}{rc_{33}} & -\dfrac{nc_{13}}{rc_{33}} & -\dfrac{2\mathrm{i}m\pi c_{23}}{Lc_{33}} \\ \dfrac{n}{r} & \dfrac{1}{r} & 0 \\ -\dfrac{2\mathrm{i}m\pi}{L} & 0 & 0 \end{bmatrix}, \qquad \mathbf{g}_{nm}^{(1,2)} = \begin{bmatrix} \dfrac{1}{c_{33}} & 0 & 0 \\ 0 & \dfrac{1}{c_{55}} & 0 \\ 0 & 0 & \dfrac{1}{c_{44}} \end{bmatrix}, \qquad \mathbf{g}_{nm}^{(2,2)} = \begin{bmatrix} \dfrac{c_{13}-c_{33}}{rc_{33}} & -\dfrac{n}{r} & -\dfrac{2\mathrm{i}m\pi}{L} \\ \dfrac{nc_{13}}{rc_{33}} & -\dfrac{2}{r} & 0 \\ -\dfrac{2\mathrm{i}m\pi c_{23}}{Lc_{33}} & 0 & -\dfrac{1}{r} \end{bmatrix},$$

$$\mathbf{g}_{nm}^{(2,1)} = \begin{bmatrix} \dfrac{c_{11}}{r^2}-\dfrac{c_{13}^2}{r^2c_{33}}+s^2\rho_o & \dfrac{\Upsilon}{r^2c_{33}} & \dfrac{2\mathrm{i}\Omega}{Lrc_{33}} \\ \dfrac{n\Upsilon}{r^2c_{33}} & \dfrac{n\Upsilon}{r^2c_{33}}+\dfrac{4m^2\pi^2c_{66}}{L^2}+s^2\rho_o & \dfrac{2\mathrm{i}\varsigma}{Lrc_{33}} \\ \dfrac{2\mathrm{i}\Omega}{Lrc_{33}} & -\dfrac{2\mathrm{i}\varsigma}{Lrc_{33}} & \dfrac{4m^2\pi^2(-c_{23}^2+c_{22}c_{33})}{L^2c_{33}}+\dfrac{n^2c_{66}}{r^2}+s^2\rho_o \end{bmatrix},$$

and

$$\mathbf{G}_{nm}^{(1,1)} = \begin{bmatrix} -\dfrac{\beta_1}{r\beta_3} \\ \dfrac{n}{r} \\ -\dfrac{2\mathrm{i}m\pi}{L} \\ \dfrac{1}{r^2\beta_3}(-C_{13}\beta_1-\chi_1e_{33}+\mu_1)+s^2\rho_{\mathrm{P}} \end{bmatrix}, \qquad \mathbf{G}_{nm}^{(1,2)} = \begin{bmatrix} -\dfrac{\mathrm{i}n\beta_1}{r\beta_3} \\ \dfrac{1}{r} \\ 0 \\ \dfrac{\mathrm{i}n}{r^2\beta_3}(-e_{33}\chi_1-C_{13}\beta_1+\mu_1) \end{bmatrix},$$

$$\mathbf{G}_{nm}^{(1,3)} = \begin{bmatrix} -\dfrac{2\mathrm{i}m\pi\beta_2}{L\beta_3} \\ 0 \\ 0 \\ \dfrac{2\mathrm{i}m\pi}{Lr\beta_3}(e_{33}\chi_3+C_{13}\beta_2-\mu_2) \end{bmatrix}, \qquad \mathbf{G}_{nm}^{(1,4)} = \begin{bmatrix} \dfrac{\varepsilon_{33}}{\beta_3} & 0 & 0 & \dfrac{e_{33}}{\beta_3} & 0 \\ 0 & \dfrac{1}{C_{55}} & 0 & 0 & \dfrac{ne_{15}}{rC_{55}} \\ 0 & 0 & \dfrac{1}{C_{44}} & 0 & -\dfrac{2\mathrm{i}m\pi e_{24}}{LC_{44}} \\ \dfrac{\beta_1-\beta_3}{r\beta_3} & -\dfrac{n}{r} & -\dfrac{2\mathrm{i}m\pi}{L} & -\dfrac{\chi_4}{r\beta_3} & 0 \end{bmatrix},$$

$$\mathbf{G}_{nm}^{(2,1)} = \begin{bmatrix} \dfrac{n}{r^2\beta_3}(e_{33}\chi_1 + C_{13}\beta_1 - \mu_1) \\ -\dfrac{2\mathrm{i}m\pi}{Lr\beta_3}(e_{33}\chi_2 + C_{23}\beta_1 - \mu_2) \\ 0 \\ \dfrac{\chi_4}{r\beta_3} \end{bmatrix}, \qquad \mathbf{G}_{nm}^{(2,2)} = \begin{bmatrix} \dfrac{1}{L^2r^2\beta_3}[\beta_3\Psi_1 - L^2n^2(e_{31}\chi_4 + C_{13}\beta_1)] \\ -\dfrac{2\mathrm{i}mn\pi}{Lr\beta_3}(e_{33}\chi_2 + C_{23}\beta_1 - \mu_2 - C_{66}\beta_3) \\ 0 \\ \dfrac{n\chi_4}{r\beta_3} \end{bmatrix},$$

$$\mathbf{G}_{nm}^{(2,3)} = \begin{bmatrix} \dfrac{2\mathrm{i}mn\pi}{Lr\beta_3}(\mu_2 + C_{66}\beta_3 - \chi_2 - C_{23}\beta_1) \\ \dfrac{1}{L^2r^2\beta_3}[\beta_3\Psi_2 - 4m^2\pi^2r^2(e_{32}\delta + C_{23}\beta_2)] \\ 0 \\ \dfrac{2\mathrm{i}m\pi\delta}{L\beta_3} \end{bmatrix}, \qquad \mathbf{G}_{nm}^{(2,4)} = \begin{bmatrix} \dfrac{n\beta_1}{r\beta_3} & -\dfrac{2}{r} & 0 & -\dfrac{n\chi_4}{r\beta_3} & 0 \\ -\dfrac{2\mathrm{i}m\pi\beta_2}{L\beta_3} & 0 & -\dfrac{1}{r} & \dfrac{2\mathrm{i}m\pi\delta}{L\beta_3} & 0 \\ 0 & -\dfrac{ne_{15}}{rC_{55}} & -\dfrac{2\mathrm{i}m\pi e_{24}}{LC_{44}} & -\dfrac{1}{r} & \zeta \\ \dfrac{e_{33}}{\beta_3} & 0 & 0 & -\dfrac{C_{33}}{\beta_3} & 0 \end{bmatrix},$$

in which

$$\Upsilon = n(c_{13}^2 - c_{11}c_{33}), \qquad \Omega = m\pi(c_{13}c_{23} - c_{12}c_{33}), \qquad \varsigma = mn\pi[-c_{13}c_{23} + c_{33}(c_{12} + c_{66})],$$
$$\delta = C_{33}e_{32} - C_{23}e_{33}\,, \qquad \zeta = \frac{-n^2(e_{15}^2 + C_{55}\varepsilon_{11})}{r^2C_{55}} - \frac{4m^2\pi^2(e_{24}^2 + C_{44}\varepsilon_{22})}{L^2C_{44}}\,,$$
$$\chi_1 = C_{13}e_{31} - C_{11}e_{33}\,, \qquad \chi_2 = C_{13}e_{32} - C_{11}e_{33}\,, \qquad \chi_3 = C_{23}e_{31} - C_{12}e_{33}\,, \qquad \chi_4 = C_{33}e_{31} - C_{13}e_{33}\,,$$
$$\Psi_1 = L^2n^2C_{11} + r^2(4m^2\pi^2C_{66} + L^2s^2\rho_{\mathrm{P}}), \qquad \Psi_2 = L^2n^2C_{66} + r^2(4m^2\pi^2C_{22} + L^2s^2\rho_{\mathrm{P}}),$$
$$\beta_i = e_{3i}e_{33} + C_{i3}\varepsilon_{33} \quad (i = 1,2,3) \qquad \mu_i = C_{33}(e_{31}e_{3i} + C_{1i}\varepsilon_{33}) \quad (i = 1,2).$$

Appendix C

$$\mathbf{A}_{nm}^{\mathrm{c1}} = \begin{bmatrix} \mathrm{W}_{\mathrm{c1},nm}^{(1,1)} + Q_{nm}^{\mathrm{in}}\mathrm{W}_{\mathrm{c1},nm}^{(1,4)} & \mathrm{W}_{\mathrm{c1},nm}^{(1,2)} & \mathrm{W}_{\mathrm{c1},nm}^{(1,3)} & -1 & 0 & 0 & \mathrm{W}_{\mathrm{c1},nm}^{(1,7)} & 0 \\ \mathrm{W}_{\mathrm{c1},nm}^{(2,1)} + Q_{nm}^{\mathrm{in}}\mathrm{W}_{\mathrm{c1},nm}^{(2,4)} & \mathrm{W}_{\mathrm{c1},nm}^{(2,2)} & \mathrm{W}_{\mathrm{c1},nm}^{(2,3)} & 0 & -1 & 0 & \mathrm{W}_{\mathrm{c1},nm}^{(2,7)} & 0 \\ \mathrm{W}_{\mathrm{c1},nm}^{(3,1)} + Q_{nm}^{\mathrm{in}}\mathrm{W}_{\mathrm{c1},nm}^{(3,4)} & \mathrm{W}_{\mathrm{c1},nm}^{(3,2)} & \mathrm{W}_{\mathrm{c1},nm}^{(3,3)} & 0 & 0 & -1 & \mathrm{W}_{\mathrm{c1},nm}^{(3,7)} & 0 \\ \mathrm{W}_{\mathrm{c1},nm}^{(4,1)} + Q_{nm}^{\mathrm{in}}\mathrm{W}_{\mathrm{c1},nm}^{(4,4)} & \mathrm{W}_{\mathrm{c1},nm}^{(4,2)} & \mathrm{W}_{\mathrm{c1},nm}^{(4,3)} & -Q_{nm}^{\mathrm{ex}} & 0 & 0 & \mathrm{W}_{\mathrm{c1},nm}^{(4,7)} & 0 \\ \mathrm{W}_{\mathrm{c1},nm}^{(5,1)} + Q_{nm}^{\mathrm{in}}\mathrm{W}_{\mathrm{c1},nm}^{(5,4)} & \mathrm{W}_{\mathrm{c1},nm}^{(5,2)} & \mathrm{W}_{\mathrm{c1},nm}^{(5,3)} & 0 & 0 & 0 & \mathrm{W}_{\mathrm{c1},nm}^{(5,7)} & 0 \\ \mathrm{W}_{\mathrm{c1},nm}^{(6,1)} + Q_{nm}^{\mathrm{in}}\mathrm{W}_{\mathrm{c1},nm}^{(6,4)} & \mathrm{W}_{\mathrm{c1},nm}^{(6,2)} & \mathrm{W}_{\mathrm{c1},nm}^{(6,3)} & 0 & 0 & 0 & \mathrm{W}_{\mathrm{c1},nm}^{(6,7)} & 0 \\ \mathrm{W}_{\mathrm{c1},nm}^{(7,1)} + Q_{nm}^{\mathrm{in}}\mathrm{W}_{\mathrm{c1},nm}^{(7,4)} & \mathrm{W}_{\mathrm{c1},nm}^{(7,2)} & \mathrm{W}_{\mathrm{c1},nm}^{(7,3)} & 0 & 0 & 0 & \mathrm{W}_{\mathrm{c1},nm}^{(7,7)} & -1 \\ \mathrm{W}_{\mathrm{c1},nm}^{(8,1)} + Q_{nm}^{\mathrm{in}}\mathrm{W}_{\mathrm{c1},nm}^{(8,4)} & \mathrm{W}_{\mathrm{c1},nm}^{(8,2)} & \mathrm{W}_{\mathrm{c1},nm}^{(8,3)} & -\kappa_{\mathrm{p}} - \kappa_{\mathrm{v}} & 0 & 0 & \mathrm{W}_{\mathrm{c1},nm}^{(8,7)} & 0 \end{bmatrix},$$

$$\mathbf{A}_{nm}^{\mathrm{c2}} = \begin{bmatrix} \mathbf{Z}_{nm}^{(1,1)} & \mathbf{Z}_{nm}^{(1,2)} & \mathbf{Z}_{nm}^{(1,3)} & \mathbf{Z}_{nm}^{(1,4)} \\ \mathbf{Z}_{nm}^{(2,1)} & \mathbf{Z}_{nm}^{(2,2)} & \mathbf{Z}_{nm}^{(2,3)} & \mathbf{Z}_{nm}^{(2,4)} \\ \mathbf{Z}_{nm}^{(3,1)} & \mathbf{Z}_{nm}^{(3,2)} & \mathbf{Z}_{nm}^{(3,3)} & \mathbf{Z}_{nm}^{(3,4)} \\ \mathbf{Z}_{nm}^{(4,1)} & \mathbf{Z}_{nm}^{(4,2)} & \mathbf{Z}_{nm}^{(4,3)} & \mathbf{Z}_{nm}^{(4,4)} \end{bmatrix},$$

where $\mathrm{W}_{ck,nm}^{(i,j)}$ $(k = 1,2)$ refer to the (i,j)-th element of the global transfer matrix $\mathbf{W}_{nm}^{ck}(s)$ associated with the k-th configuration. Also,

$$\mathbf{Z}_{nm}^{(1,1)} = \begin{bmatrix} \mathrm{W}_{\mathrm{c2},nm}^{(1,1)} + Q_{nm}^{\mathrm{in}}\mathrm{W}_{\mathrm{c2},nm}^{(1,4)} & \mathrm{W}_{\mathrm{c2},nm}^{(1,2)} & \mathrm{W}_{\mathrm{c2},nm}^{(1,3)} \\ \mathrm{W}_{\mathrm{c2},nm}^{(2,1)} + Q_{nm}^{\mathrm{in}}\mathrm{W}_{\mathrm{c2},nm}^{(2,4)} & \mathrm{W}_{\mathrm{c2},nm}^{(2,2)} & \mathrm{W}_{\mathrm{c2},nm}^{(2,3)} \\ \mathrm{W}_{\mathrm{c2},nm}^{(3,1)} + Q_{nm}^{\mathrm{in}}\mathrm{W}_{\mathrm{c2},nm}^{(3,4)} & \mathrm{W}_{\mathrm{c2},nm}^{(3,2)} & \mathrm{W}_{\mathrm{c2},nm}^{(3,3)} \end{bmatrix}, \qquad \mathbf{Z}_{nm}^{(1,2)} = \begin{bmatrix} -1 & 0 \\ 0 & -1 \\ 0 & 0 \end{bmatrix},$$

$$\mathbf{Z}_{nm}^{(1,3)} = \begin{bmatrix} 0 & \mathrm{W}_{\mathrm{c2},nm}^{(1,8)} & \mathrm{W}_{\mathrm{c2},nm}^{(1,9)} \\ 0 & \mathrm{W}_{\mathrm{c2},nm}^{(2,8)} & \mathrm{W}_{\mathrm{c2},nm}^{(2,9)} \\ -1 & \mathrm{W}_{\mathrm{c2},nm}^{(3,8)} & \mathrm{W}_{\mathrm{c2},nm}^{(3,9)} \end{bmatrix}, \qquad \mathbf{Z}_{nm}^{(1,4)} = \begin{bmatrix} 0 & 0 \\ 0 & 0 \\ 0 & 0 \end{bmatrix},$$

$$\mathbf{Z}_{nm}^{(2,1)} = \begin{bmatrix} \mathrm{W}_{\mathrm{c2},nm}^{(4,1)} + Q_{nm}^{\mathrm{in}}\mathrm{W}_{\mathrm{c2},nm}^{(4,4)} & \mathrm{W}_{\mathrm{c2},nm}^{(4,2)} & \mathrm{W}_{\mathrm{c2},nm}^{(4,3)} \\ \mathrm{W}_{\mathrm{c2},nm}^{(5,1)} + Q_{nm}^{\mathrm{in}}\mathrm{W}_{\mathrm{c2},nm}^{(5,4)} & \mathrm{W}_{\mathrm{c2},nm}^{(5,2)} & \mathrm{W}_{\mathrm{c2},nm}^{(5,3)} \end{bmatrix}, \qquad \mathbf{Z}_{nm}^{(2,2)} = \begin{bmatrix} -Q_{nm}^{\mathrm{ex}} & 0 \\ 0 & 0 \end{bmatrix},$$

$$\mathbf{Z}_{nm}^{(2,3)} = \begin{bmatrix} 0 & \mathrm{W}_{\mathrm{c2},nm}^{(4,8)} & \mathrm{W}_{\mathrm{c2},nm}^{(4,9)} \\ 0 & \mathrm{W}_{\mathrm{c2},nm}^{(5,8)} & \mathrm{W}_{\mathrm{c2},nm}^{(5,9)} \end{bmatrix}, \qquad \mathbf{Z}_{nm}^{(2,4)} = \begin{bmatrix} 0 & 0 \\ 0 & 0 \end{bmatrix},$$

$$\mathbf{Z}_{nm}^{(3,1)} = \begin{bmatrix} \mathrm{W}_{\mathrm{c2},nm}^{(6,1)} + Q_{nm}^{\mathrm{in}}\mathrm{W}_{\mathrm{c2},nm}^{(6,4)} & \mathrm{W}_{\mathrm{c2},nm}^{(6,2)} & \mathrm{W}_{\mathrm{c2},nm}^{(6,3)} \\ \mathrm{W}_{\mathrm{c2},nm}^{(7,1)} + Q_{nm}^{\mathrm{in}}\mathrm{W}_{\mathrm{c2},nm}^{(7,4)} & \mathrm{W}_{\mathrm{c2},nm}^{(7,2)} & \mathrm{W}_{\mathrm{c2},nm}^{(7,3)} \\ \mathrm{W}_{\mathrm{c2},nm}^{(8,1)} + Q_{nm}^{\mathrm{in}}\mathrm{W}_{\mathrm{c2},nm}^{(8,4)} & \mathrm{W}_{\mathrm{c2},nm}^{(8,2)} & \mathrm{W}_{\mathrm{c2},nm}^{(8,3)} \end{bmatrix}, \qquad \mathbf{Z}_{nm}^{(3,2)} = \begin{bmatrix} 0 & 0 \\ 0 & 0 \\ 0 & 0 \end{bmatrix},$$

$$\mathbf{Z}_{nm}^{(3,3)} = \begin{bmatrix} 0 & \mathrm{W}_{\mathrm{c2},nm}^{(6,8)} & \mathrm{W}_{\mathrm{c2},nm}^{(6,9)} \\ 0 & \mathrm{W}_{\mathrm{c2},nm}^{(7,8)} & \mathrm{W}_{\mathrm{c2},nm}^{(7,9)} \\ 0 & \mathrm{W}_{\mathrm{c2},nm}^{(8,8)} - \kappa_{\phi} - \kappa_{\dot{\phi}} & \mathrm{W}_{\mathrm{c2},nm}^{(8,9)} \end{bmatrix}, \qquad \mathbf{Z}_{nm}^{(3,4)} = \begin{bmatrix} 0 & 0 \\ -1 & 0 \\ 0 & 0 \end{bmatrix},$$

$$\mathbf{Z}_{nm}^{(4,1)} = \begin{bmatrix} \mathrm{W}_{\mathrm{c2},nm}^{(9,1)} + Q_{nm}^{\mathrm{in}}\mathrm{W}_{\mathrm{c2},nm}^{(9,4)} & \mathrm{W}_{\mathrm{c2},nm}^{(9,2)} & \mathrm{W}_{\mathrm{c2},nm}^{(9,3)} \\ \mathrm{W}_{\mathrm{c2},nm}^{(10,1)} + Q_{nm}^{\mathrm{in}}\mathrm{W}_{\mathrm{c2},nm}^{(10,4)} & \mathrm{W}_{\mathrm{c2},nm}^{(10,2)} & \mathrm{W}_{\mathrm{c2},nm}^{(10,3)} \end{bmatrix}, \qquad \mathbf{Z}_{nm}^{(4,2)} = \begin{bmatrix} 0 & 0 \\ 0 & 0 \end{bmatrix},$$

$$\mathbf{Z}_{nm}^{(4,3)} = \begin{bmatrix} 0 & \mathrm{W}_{\mathrm{c2},nm}^{(9,8)} & \mathrm{W}_{\mathrm{c2},nm}^{(9,9)} \\ 0 & \mathrm{W}_{\mathrm{c2},nm}^{(10,8)} & \mathrm{W}_{\mathrm{c2},nm}^{(10,9)} \end{bmatrix}, \qquad \mathbf{Z}_{nm}^{(4,4)} = \begin{bmatrix} 0 & -1 \\ 0 & 0 \end{bmatrix}.$$

Also

$$\mathbf{b}_{nm}^{\mathrm{c1}} = \begin{bmatrix} -\mathrm{W}_{\mathrm{c1},nm}^{(1,4)}F_{\mathrm{in}}^{nm} \\ -\mathrm{W}_{\mathrm{c1},nm}^{(2,4)}F_{\mathrm{in}}^{nm} \\ -\mathrm{W}_{\mathrm{c1},nm}^{(3,4)}F_{\mathrm{in}}^{nm} \\ F_{\mathrm{ex}}^{nm} - \mathrm{W}_{\mathrm{c1},nm}^{(4,4)}F_{\mathrm{in}}^{nm} \\ -\mathrm{W}_{\mathrm{c1},nm}^{(5,4)}F_{\mathrm{in}}^{nm} \\ -\mathrm{W}_{\mathrm{c1},nm}^{(6,4)}F_{\mathrm{in}}^{nm} \\ -\mathrm{W}_{\mathrm{c1},nm}^{(7,4)}F_{\mathrm{in}}^{nm} \\ -\mathrm{W}_{\mathrm{c1},nm}^{(8,4)}F_{\mathrm{in}}^{nm} \end{bmatrix}, \qquad \mathbf{b}_{nm}^{\mathrm{c2}} = \begin{bmatrix} -\mathrm{W}_{\mathrm{c2},nm}^{(1,4)}F_{\mathrm{in}}^{nm} \\ -\mathrm{W}_{\mathrm{c2},nm}^{(2,4)}F_{\mathrm{in}}^{nm} \\ -\mathrm{W}_{\mathrm{c2},nm}^{(3,4)}F_{\mathrm{in}}^{nm} \\ F_{\mathrm{ex}}^{nm} - \mathrm{W}_{\mathrm{c2},nm}^{(4,4)}F_{\mathrm{in}}^{nm} \\ -\mathrm{W}_{\mathrm{c2},nm}^{(5,4)}F_{\mathrm{in}}^{nm} \\ -\mathrm{W}_{\mathrm{c2},nm}^{(6,4)}F_{\mathrm{in}}^{nm} \\ -\mathrm{W}_{\mathrm{c2},nm}^{(7,4)}F_{\mathrm{in}}^{nm} \\ -\mathrm{W}_{\mathrm{c2},nm}^{(8,4)}F_{\mathrm{in}}^{nm} \\ -\mathrm{W}_{\mathrm{c2},nm}^{(9,4)}F_{\mathrm{in}}^{nm} \\ -\mathrm{W}_{\mathrm{c2},nm}^{(10,4)}F_{\mathrm{in}}^{nm} \end{bmatrix}.$$

References

1. ABAQUS, Analysis User's Manual Version 6.11 Online Documentation.
2. Alkhatib R., Golnaraghi M.F. (2003), *Active structural vibration control: a review*, The Shock and Vibration Digest, **35**, 367–383.
3. Babaev A.E., Babaev A.A. (2005), *Generation of nonstationary waves by a thick-walled piezoceramic cylinder excited by electric signals*, IEEE Transactions on Ultrasonics Ferroelectrics and Frequency Control, **52**, 518–524.
4. Babaev A.E., Babaev A.A., Yanchevskiy I.V. (2010), *Influence of an oscillating circuit on the radiation of transient acoustic waves by an electroelastic cylinder*, Journal of the Acoustical Society of America, **127**, 2282–2289.
5. Balabaev S.M., Ivina N.F. (1999), *Acoustic radiation of a cylindrical piezoceramic transducer with solid internal filling*, Acoustical Physics, **45**, 398–401.
6. Bélanger P.R. (1995), *Control Engineering: A Modern Approach*, Oxford University Press, London.
7. Bruch J.J.C., Sloss J.M., Adali S., Sadek I.S. (2000), *Optimal piezo-actuator locations/lengths and*

applied voltage for shape control of beams, Smart Materials and Structures, **9**, 205–211.

8. Cao X.T., Shi L., Zhang X., Jiang G. (2013), *Active control of acoustic radiation from laminated cylindrical shells integrated with a piezoelectric layer*, Smart Materials and Structures, **22**, 964–1726.

9. Cao Y., Sun H., An F., Li X. (2012), *Active control of low-frequency sound radiation by cylindrical shell with piezoelectric stack force actuators*, Journal of Sound and Vibration, **331**, 2471–2484.

10. Caresta M. (2011), *Active control of sound radiated by a submarine in bending vibration*, Journal of Sound and Vibration, **330**, 615–24.

11. Chen W.Q., Bian Z.G., Ding H.J. (2004), *Three dimensional vibration analysis of fluid filled orthotropic FGM cylindrical shells*, International Journal of Mechanical Science, **46**, 159–171.

12. Chen W.Q., Bian Z.G., Lv C.F., Ding H.J. (2004), *3D Free vibration analysis of a functionally graded piezoelectric hollow cylinder filled with compressible fluid*, International Journal of Solids and Structures, **41**, 947–964.

13. Chopra I. (2002), *Review of state of art of smart structures and integrated systems*, AIAA Journal, **11**, 2145–2187.

14. Clark R.L., Fuller C.R. (1994), *Active control of structurally radiated sound from an enclosed finite cylinder*, Journal of Intelligent Material Systems and Structures, **5**, 379–391.

15. Crawley E.F., de Luis J. (1987), *Use of piezoelectric actuators as elements of intelligent structures*, The American Institute of Aeronautics and Astronautics, **25**, 1373–1385.

16. Ding H.J., Chen W.Q., Gue Y.M., Yang Q.D. (1997), *Free vibrations of piezoelectric cylindrical shells filled with compressible fluid*, International Journal of Solids and Structures, **34**, 2025–2034.

17. Ding H.J., Chen W.Q. (2001), *Three Dimensional Problems of Piezoelectricity*, Nova Science Publishers, New York.

18. Durbin F. (1973), *Numerical inversion of Laplace transforms: an effective improvement of Dubner and Abate's method*, Computer Journal, **17**, 371–376.

19. Fan S.C., Li S.M., Yu G.Y. (2005), *Dynamic fluid-structure interaction analysis using boundary finite element method-finite element method*, Journal of Applied Mechanics, **72**, 591–598.

20. Gabbert U., Tzou H.S. (2001), *Smart Structures and Structronic Systems*, Kluwer, Dordrect.

21. Genetic Algorithm Toolbox Available http://www.mathworks.com/products/global-optimization/description4.html

22. Hasheminejad S.M., Alaei-Varnosfaderani M. (2012), *Vibroacoustic response and active control of a fluid-filled functionally graded piezoelectric material composite cylinder*, Journal of Intelligent Material Systems and Structures, **23**, 775–790.

23. Hasheminejad S.M., Alaei-Varnosfaderani M. (2013), *Acoustic radiation and active control from a smart functionally graded submerged hollow cylinder*, Journal of Vibration and Control, doi:10.1177/1077546313483787.

24. Hasheminejad S.M., Bahari A., Abbasion S. (2011), *Modelling and simulation of acoustic pulse interaction with a fluid-filled hollow elastic sphere through numerical Laplace inversion*, Applied Mathematical Modelling, **35**, 22–49.

25. Hasheminejad S.M., Kazemirad S. (2008), *Dynamic viscoelastic effects on sound wave scattering by an eccentric compound circular cylinder*, Journal of Sound and Vibration, **318**, 506–526.

26. Hasheminejad S.M., Keshavarzpour H. (2013), *Active sound radiation control of a thick piezolaminated smart rectangular plate*, Journal of Sound and Vibration, **332**, 4798–4816.

27. Hasheminejad S.M., Mohammadi M.M., Jarrahi M. (2013), *Liquid sloshing in partly-filled laterally-excited circular tanks equipped with baffles*, Journal of Fluids and Structures, in press.

28. Hasheminejad S.M., Mousavi-akbarzadeh H. (2012), *Vibroacoustic response of an eccentric hollow cylinder*, Journal of Sound and Vibration, 331, 3791–3808.

29. Hasheminejad S.M., Mousavi-akbarzadeh H. (2013), *Three dimensional non-axisymmetric transient acoustic radiation from an eccentric hollow cylinder*, Wave Motion, 50, 723–738.

30. Hasheminejad S.M., Mousavi-akbarzadeh H. (2015), *Transient acoustic radiation from an eccentric sphere*, Applied Mathematical Modelling, in press, doi:10.1016/j.apm.2015.04.010.

31. Hasheminejad S.M., Rajabi M. (2008), *Scattering and active acoustic control from a submerged piezoelectric-coupled orthotropic hollow cylinder*, Journal of Sound and Vibration, **318**, 50–73.

32. Hasheminejad S.M., Shakeri R., Rezaei S. (2012), *Vibro-acoustic response of an elliptical plate-cavity coupled system to external shock loads*, Applied Acoustics, **73**, 757–769.

33. Hasheminejad S.M., Shahsavarifard A., Shahsavarifard M. (2008), *Dynamic Viscoelastic Effects on Free Vibrations of a Submerged Fluid-filled Thin Cylindrical Shell*, Journal of Vibration and Control, **14**, 849–865.

34. Hilderbrand F.B. (1992), *Methods of Applied Mathematics*, Dover, New York.

35. Honarvar F., Enjilela S., Sinclair A.N. (2011), *Correlation between helical surface waves and guided modes of an infinite immersed elastic cylinder*, Ultrasonics, **51**, 238–244.

36. Iakovlev S., Santos H.A.F.A., Williston K., Murray R., Mitchell M. (2012), *Non-stationary radiation by a cylindrical shell: Numerical modeling using the Reissner-Mindlin theory*, Journal of Fluids and Structures, **36**, 50–69.

37. Iakovlev S., Seaton C.T., Sigrist J.F. (2013), *Submerged circular cylindrical shell subjected to two consecutive shock waves: Resonance-like phenomena*, Journal of Fluids and Structures, **24**, 70–87.

38. Jin G., Liu X., Liu Z., Yang T. (2011), *Active control of structurally radiated sound from an elastic cylindrical shell*, Journal of Marine Science and Application, **10**, 88–97.

39. Kim H.S., Sohn J.W., Jeon J., Choi S.B. (2013), *Reduction of the radiating sound of a submerged finite cylindrical shell structure by active vibration control*, Sensors, **13**, 2131–2147.

40. Kumar S.R., Ray M.C. (2013), *Active control of geometrically nonlinear vibrations of doubly curved smart sandwich shells using 1–3 piezoelectric composites*, Composite Structures, **105**, 173–187.

41. Kwak M.K., Yang D.H., Lee J.H. (2012), *Active vibration control of a submerged cylindrical shell by piezoelectric sensors and actuators*, Proceedings of SPIE – The International Society for Optical Engineering, 8341, 83412F.

42. Kwak M.K., Yang D.H. (2013), *Active vibration control of a ring-stiffened cylindrical shell in contact with unbounded external fluid and subjected to harmonic disturbance by piezoelectric sensor and actuator*, Journal of Sound and Vibration, **332**, 4775–4797.

43. Laplante W., Chen T.H., Baz A., Shields W. (2002), *Active control of vibration and noise radiation from fluid-loaded cylinder using active constrained layer damping*, Journal of Vibration and Control, **8**, 877–902.

44. Leblond C., Sigrist J.F. (2010), *A versatile approach to the study of the transient response of a submerged thin shell*, Journal of Sound and Vibration, **329**, 56–71.

45. Lester H.C., Lefebvre S. (1993), *Piezoelectric actuator models for active sound and vibration control of cylinders*, Journal of Intelligent Material Systems and Structures, **4**, 295–306.

46. Maillard J.P., Fuller C.R. (1999), *Active control of sound radiation from cylinders with piezoelectric actuators and structural acoustic sensing*, Journal of Sound and Vibration, **222**, 363–388.

47. Morgan Matroc Incorporated (1993), Guide to Modern Piezoelectric Ceramics, Electro Ceramics Division.

48. Niezrecki C., Cudney H.H. (2001), *Feasibility to control launch vehicle internal acoustic using piezoelectric actuators*, Journal of Intelligent Material Systems and Structures, **12**, 647–660.

49. Pan X., Tso Y., Juniper R. (2008), *Active control of low-frequency hull-radiated noise*, Journal of Sound and Vibration, **313**, 29–45.

50. Parallel Computing Toolbox MATLAB Available: http://www.mathworks.com/products/parallel-computing/.

51. Pierce A.D. (1991), *Acoustics: An Introduction to its Physical Principles and Applications*, American Institute of Physics, New York.

52. Ray M.C., Reddy J.N. (2013), *Active damping of laminated cylindrical shells conveying ?uid using 1–3 piezoelectric composites*, Composite Structures, **98**, 261–271.

53. Ruzzene M., Baz A. (2000), *Active/passive control of sound radiation and power flow in fluid-loaded shells*, Thin-Walled Structures, **38**, 17–42.

54. Sarangi S.K., Ray M.C. (2011), *Active damping of geometrically nonlinear vibrations of laminated composite shallow shells using vertically/obliquely reinforced 1–3 piezoelectric composites*, International Journal of Mechanics and Materials in Design, **7**, 29–44.

55. Shen H., Wen J., Yu D., Asgari M., Wen X. (2013), *Control of sound and vibration of fluid-filled cylindrical shells via periodic design and active control*, Journal of Sound and Vibration, **332**, 4193–4209.

56. Song K., Atalla M.J., Steven R.H. (June 19, 2000), *Active structural acoustic control of a thick-walled cylindrical shell*, Proc. SPIE 3984, Smart Structures and Materials 2000: Mathematics and Control in Smart Structures, 112, doi:10.1117/12.388756.

57. Su D., Zhang Q., Zhu S. (2010), *Attenuation of Structurally Radiated Sound from an Elastic Cylindrical Shell by Local Vibration Control*, Key Engineering Materials, **450**, 494–497.

58. Su Y.C., Ma C.C. (2012), *Transient wave analysis of a cantilever Timoshenko beam subjected to impact loading by Laplace transform and normal mode methods*, International Journal of Solids and Structures, **49**, 1158–1176.

59. Thorp O., Ruzzene M., Baz A. (2005), *Attenuation of wave propagation in fluid-loaded shells with periodic shunted piezoelectric rings*, Smart Material and Structures, **14**, 594–604.

60. Überall H. (2001), *Acoustics of shells*, Acoustical Physics, **47**, 115–139.

61. Vel S.S., Baillargeon B.P. (2005), *Analysis of static deformation vibration and active damping of cylindrical composite shells with piezoelectric shear actuators*, Journal of Vibration and Acoustics, **127**, 395–407.

62. Vovk I.V., Oliynik V.N. (1996), *Sound radiation by a cylindrical piezoelastic shell with an asymmetric insertion*, Journal of the Acoustical Society of America, **99**, 133–138.

63. Wang Y.F., Berger B.S. (1971), *Dynamic interaction between an elastic cylindrical shell subjected to point loadings and an acoustic medium*, The Journal of the Acoustical Society of America, **49**, 293–298.

64. Wang C.Y., Vaicaitis R. (1998), *Active control of vibrations and noise of double wall cylindrical shells*, Journal of Sound and Vibration, **216**, 865–888.

65. Wilson O.B. (1988), *Introduction to the Theory and Design of Sonar Transducers*, Naval Sea Systems Command, Washington DC.

66. Xiang Y., Yuan L., Huang Y., Ni Q. (2011), *A novel matrix method for coupled vibration and damping effect analyses of liquid-filled circular cylindrical shells with partially constrained layer damping under harmonic excitation*, Applied Mathematical Modeling, **35**, 2209–222.

67. Yu J., Wu B., Chen G. (2009), *Wave characteristics in functionally graded piezoelectric hollow cylinders*, Archive of Applied Mechanics, **79**, 807–824.

68. Zhang Y., Tong Z.P., Zhangi Z.Y., Hua H.X. (2006), *Finite element modeling of a fluid-filled cylindrical shell with piezoelectric damping*, Journal of Vibration Engineering, **19**, 24–30.

69. http://www.mediafire.com/download/4s2ciq8ldqjsvgb/SequenceFicker.mp4 (Accessed 30 May 2015) Animation: Effect of control action on the internal/external transient sound pressure fields due to an impulsive pair of diametrical external point loads acting on the piezo-composite cylinder in the second configuration (Config. 2).